



### Available online at www.sciencedirect.com

# **ScienceDirect**

Comput. Methods Appl. Mech. Engrg. 415 (2023) 116206

Computer methods in applied mechanics and engineering

www.elsevier.com/locate/cma

# A peridynamic model for advection-reaction-diffusion problems

Chenwen Tian<sup>a</sup>, Shuaiqi Fan<sup>a</sup>, Juan Du<sup>b</sup>, Zhikun Zhou<sup>a</sup>, Ziguang Chen<sup>a,c,\*</sup>, Florin Bobaru<sup>d</sup>

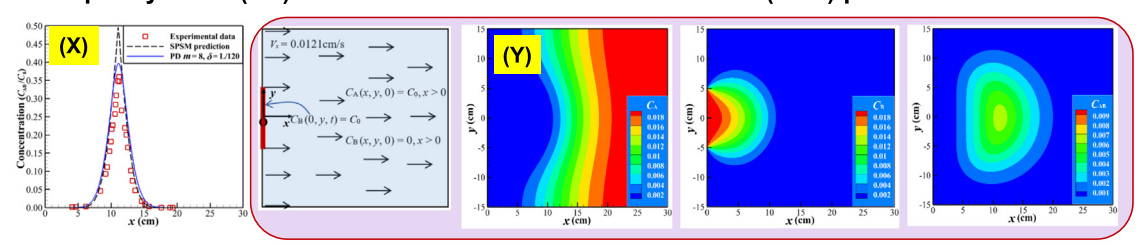
<sup>a</sup> Department of Engineering Mechanics, School of Aerospace Engineering, Huazhong University of Science and Technology, Wuhan, 430074, China

b Science and Technology on Reactor System Design Technology Laboratory, Nuclear Power Institute of China, Chengdu 610213, China c Hubei Key Laboratory of Engineering Structural Analysis and Safety Assessment, 1037 Luoyu Road, Wuhan, 430074, China d Department of Mechanical and Materials Engineering, University of Nebraska-Lincoln, Lincoln, NE, 68588-0526, USA

> Received 6 March 2023; received in revised form 19 June 2023; accepted 21 June 2023 Available online xxxx

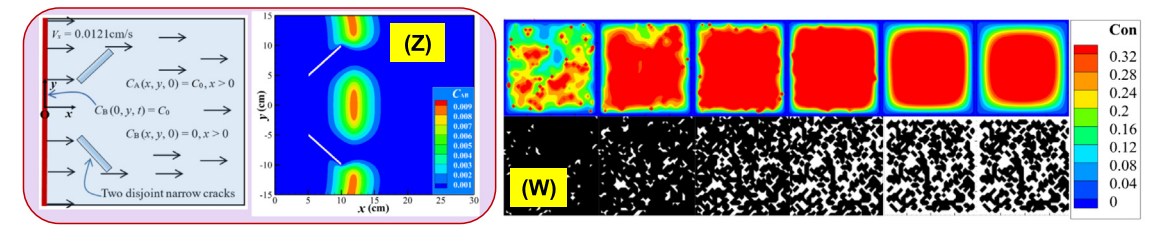
### **Graphical Abstract**

# A peridynamic (PD) model for advection-reaction-diffusion (ARD) problems



Bimolecular reactions: (X) validation of the PD ARD model in 1D; (Y) PD results for ARD in homogeneous, and (Z) inhomogeneous (slit-like sinks) 2D domains.

**Hydrolysis reaction and out-Diffusion: (W)** PD results of hydrolysis: (top row) evolution of monomer concentration distribution; (bottom row) evolution of remaining un-hydrolyzed matrix (black).



# Abstract

In this paper, a bond-based peridynamic (PD) advection-reaction-diffusion model is formulated to simulate processes involving chemical reactions, flows, and diffusion. In the formulation, the reaction rate, represented by a body force-like local

E-mail address: zchen@hust.edu.cn (Z. Chen).

<sup>\*</sup> Corresponding author at: Department of Engineering Mechanics, School of Aerospace Engineering, Huazhong University of Science and Technology, Wuhan, 430074, China.

term, depends on the local concentrations of the reactants, and the dependence varies according to the reaction type. Both linear and nonlinear dependencies are considered. A system of coupled PD equations for each substance is solved numerically. We verify and validate the PD advection–reaction–diffusion model by comparing results with those from a corresponding classical model and from experiments in both 1D and 2D, for a bimolecular reaction  $(A+B\to AB)$  in a flowing aqueous environment, similar to purifying polluted water flowing in a channel, via chemical reactions. The model is also used to simulate bimolecular advection–reaction–diffusion in heterogeneous media with impermeable inclusions, and to simulate polymer degradation through hydrolysis and diffusion, similar to how biodegradable polymer implants dissolve. © 2023 Elsevier B.V. All rights reserved.

Keywords: Peridynamics; Reaction-diffusion; Bimolecular reaction; Hydrolysis; Water pollution; Simulation

### 1. Introduction

The classical reaction–diffusion equation [1] describes the concentration evolution of one or more chemical substances due to local chemical reactions and diffusion. Reaction–diffusion processes are universal in chemistry, biology, and environmental sciences, exemplified by: changes in substance concentration in chemical reactions [2], heat conduction and mass diffusion [3], and invasive species in biology [4]. The classical reaction–diffusion equations have been used to describe the diffusion of pollutants in groundwater [5], transport of medication in human tissues, cell differentiation and growth [6], and other common practical problems [7]. When advection is important, an advection term is included in the reaction–diffusion equation, leading to a more general form, the advection–reaction–diffusion (ARD) equation [8]. A few special cases of ARD equations can be solved analytically. The rest of the problems need to use numerical approximations to find solutions. Methods like the Finite Element Method (FEM) [9], the Finite Difference Method (FDM) [10], and the Boundary Element Method (BEM) [11,12] have been commonly used to obtain approximate numerical solutions for the ARD equations. The classical/local model for ARD problems, however, cannot capture some more general behavior, such as anomalous diffusion observed in heterogeneous environments [13], long-range inhibition in biological pattern formation [6,14], and heat transport in microscale and nanoscale devices [15–17], in all of which nonlocal effects play an important role.

Peridynamics (PD), a new nonlocal theory introduced by Silling [18], has been increasingly gaining attention from academia and industry since its birth in 2000. In PD, each material point interacts with all surrounding points within a certain distance, while in classical theory, material points only interact through direct contact. The region of nonlocal interaction surrounding a material point is the PD "horizon region", normally taken as a sphere in 3D, a circular disk in 2D, or a segment in 1D. The radius of the sphere or the disk is also called the "horizon", and from the context it will be clear whether "horizon" refers to the region or its radius. Interactions between material points are represented by PD bonds: mechanical bonds transfer mechanical forces between points, thermal bonds transfer heat between their end points, etc. While there are many nonlocal theories, some use spatial derivatives under integral operators [19]. In PD, spatial derivatives are not used, in this way avoiding singularities that appear when discontinuities form in a body due to fracture and damage [20]. The integro-differential PD equations can be solved analytically (using separation of variables, for example) in special cases set in simple domains, similar to how series solutions are obtained for corresponding partial differential equations [3,21]. For general PD problems, one needs to employ numerical methods. The one-point Gauss quadrature with direct summation has been the preferred method for discretizing PD models because it leads to a meshfree model, very well suited for capturing the evolution of fracture and damage (or other types of discontinuities) in a material [22–24]. Faster algorithms have been recently introduced based on the same discretization, but the quadrature is computed using the Fast Fourier Transform (and its inverse), exploiting the convolutional structure of the PD integral operator [25,26].

Beyond its original applications in studying mechanical behavior of materials, such as fracture in brittle materials [27–30], damage in composites materials [31–35], plastic and visco-plastic deformation [36–38], hydraulic fracturing [39], rupture of films and nanofiber networks [40,41], interactions between dislocations and cracks [42], the PD theory has been successfully applied to simulate various physical and chemical behaviors, such as heat and mass transfer [43,44], corrosion in metallic materials [45–49], phase transformation [50]. Further progress on PD diffusion models, including mathematical and theoretical analysis, has appeared [3,44,51,52].

While the original PD model was the bond-based model for elasticity and brittle damage, state-based PD models have been introduced to remove the fixed Poisson's ratio limitation bond-based models have in elasticity [53]. A

state-based PD model for diffusion [52] and for convective single-phase flow in heterogeneous porous media [54] have also been proposed, but their advantage versus bond-based models in such problems is less clear. State-based models tend to be costlier to compute, in general, than corresponding bond-based models [26]. The limitation to a fixed Poisson's ratio is the main reason for the state-based extension of bond-based PD theory in mechanical problems. In reaction–diffusion problems, such limitations do not exist. In this paper, we focus on a bond-based PD model for ARD.

Recently, Ref. [55] introduced an advection-diffusion PD model, as an extension to the PD model for diffusion [3], that can treat complex geometries with ease. In the present paper, we consider extending the PD advection-diffusion [55] model for solving ARD problems, to simulate more complex physico-chemical processes. A local/classical model for steady-state ARD problems has been introduced before [2,8,56]. An example of 1D bimolecular reactive transport flows through an isotropic and homogeneous medium was solved numerically using the traditional Partial Differential Equations-based model, and the results were compared with experiments data. These types of models, when extended to higher dimensions and applied to complex domains, have difficulties tracking the evolving interfaces (e.g. between phases). While having more flexibility in tracking evolving interfaces, phase-field models of reaction-diffusion problems [57,58] still have to employ preset functional variations across an interface, which often do not correspond to the actual physics/chemistry taking place. In contrast, PD-based models for damage or phase-change have no such restrictions, and have been shown to predict the evolution of moving interfaces with accuracy [59]. Here, we introduce a new and general PD model for transient ARD problems and use it to solve 1D and 2D problems for bimolecular reactions  $(A + B \rightarrow AB)$  in a flowing aqueous environment, similar to purifying, via chemical reactions, polluted water flowing in a channel. The model is also used to simulate bimolecular ARD in heterogeneous media with impermeable inclusions, and to simulate polymer degradation through hydrolysis and diffusion.

The paper is organized as follows: Section 2 shows the ARD PD formulation, followed by introducing the numerical method used to discretize the problem in Section 3; in Section 4, we test and validate the model with examples in 1D and 2D, by comparing the PD model solutions with the corresponding classical solutions and against experimental data, and we use the new model to simulate ARD problems in complex heterogeneous media and polymer implant degradation induced by hydrolysis; conclusions are given in Section 5.

# 2. The advection-reaction-diffusion peridynamics formulation

The PD model for advection-diffusion can be written as [55]:

$$\frac{\partial C\left(\boldsymbol{x},t\right)}{\partial t} = \int_{H_{\boldsymbol{x}}} d\left(\boldsymbol{x},\boldsymbol{x}',t\right) \frac{C\left(\boldsymbol{x}',t\right) - C\left(\boldsymbol{x},t\right)}{\left\|\boldsymbol{x}'-\boldsymbol{x}\right\|^{n}} dV_{\boldsymbol{x}'} - \int_{H_{\boldsymbol{x}}} \left(\boldsymbol{v}\left(\boldsymbol{x},\boldsymbol{x}',t\right) \cdot \frac{\boldsymbol{x}'-\boldsymbol{x}}{\left\|\boldsymbol{x}'-\boldsymbol{x}\right\|}\right) \frac{C\left(\boldsymbol{x}',t\right) - C\left(\boldsymbol{x},t\right)}{\left\|\boldsymbol{x}'-\boldsymbol{x}\right\|} dV_{\boldsymbol{x}'},$$
(1)

where C(x,t) is the concentration at material point x at time t.  $H_x$  is the horizon region of x. Material point x interacts with all of the material points (x') inside its horizon  $H_x$  (see Fig. 1).  $V_{x'}$  is the volume (area in 2D, length in 1D) of x' covered by  $H_x$ . Function d(x,x',t) is the micro-diffusivity, while v(x,x',t) is a weighted flow velocity density at x over its horizon region (see Ref. [55]). Let  $v(x,x',t) = v(x,x',t) \cdot \frac{x'-x}{\|x'-x\|}$ , be the peridynamic micro-velocity, defined as the projection of the velocity vector along the (x,x') bond. In Eq. (1), n is usually taken to be an integer, 0, 1, or 2 [22,40,43]. Ref. [3] showed that only the integrand with n=2, leads to results that converge to the classical solution in the limit of the horizon size  $\delta$  (the radius of  $H_x$ , see Fig. 1) going to zero when the relative grid-density m (the ratio between the horizon size and grid spacing) is kept as a constant (the so-called " $\delta$ -convergence"), for the PD computation with the one-point Gaussian spatial integration method. For other forms,  $\delta$ -convergence happens but the limit might not be the classical solution. In this paper we use n=2.

The micro-diffusivity function d(x, x', t) and micro-velocity parameters v(x, x', t) can have different forms to reflect horizon-scale behaviors. The following two simple forms are commonly used. The "constant" micro-diffusivity/micro-velocity:

$$d\left(\mathbf{x},\mathbf{x}',t\right) = d_0, \mathbf{v}\left(\mathbf{x},\mathbf{x}',t\right) = \mathbf{v}_0, \tag{2}$$

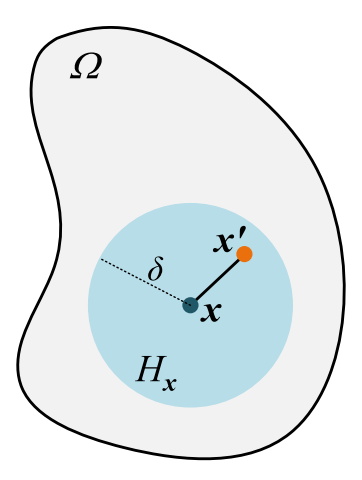


Fig. 1. Description of a PD body in 2D.

implies that the interaction between a material point and its neighboring family is independent of the bond length. The "linear" or "triangular" micro-diffusivity/micro-velocity:

$$d\left(\boldsymbol{x}, \boldsymbol{x}', t\right) = d_1 \left(1 - \frac{\|\boldsymbol{x}' - \boldsymbol{x}\|}{\delta}\right), \boldsymbol{v}\left(\boldsymbol{x}, \boldsymbol{x}', t\right) = \boldsymbol{v}_1 \left(1 - \frac{\|\boldsymbol{x}' - \boldsymbol{x}\|}{\delta}\right),$$
(3)

assumes a linear dependence on the bond length. Eqs. (2) and (3) are for time-independent micro-diffusivity/ micro-velocity. Time-dependent parameters can also be considered in the PD model (see [60]). In the examples of bimolecular synthesis reactions (see Sections 2.1, 4.1, and 4.2), we assume that all physical coefficients are time-independent, including the reaction coefficient. For the case of hydrolysis reaction (see Sections 2.2 and 4.3), the micro-diffusivity and the reaction coefficient depend on the concentration, which changes with time.

One way to determine the parameters defining the micro-diffusivity/micro-velocity in a PD model is to use calibration to classical models. For example, according to Refs. [3,55], the relationship between the micro-diffusivity d and the given classical diffusivity D, and the relationship between the micro-velocity v and the given flow velocity V can be obtained by enforcing a match between the PD solution and the classical one for the case of a linear concentration profile of chemical in a flowing media. The relationships between the physical parameters and those used in the PD model are shown in Table 1. Note that the micro-diffusivity and micro-velocity are parameters for a PD bond, which connects two material points. Therefore, the micro-diffusivity (d(x, x', t)) and micro-velocity (v(x,x',t)) depend on the classical diffusivities (D(x,t),D(x',t)) and flow velocities (V(x,t),V(x',t)) at both material points connected by the PD bond, respectively. If diffusivity and flow velocity are constant in the domain (see Sections 2.1, 4.1, and 4.2), i.e., D(x,t) = const, and V(x,t) = const, for any x, the micro-diffusivity and micro-velocity are uniform/constant for all of the PD bonds connecting points in the bulk and their values are calculated by the formulas shown in Table 1. If diffusivity, for example, is not uniform (see Sections 2.2 and 4.3), one can find the micro-diffusivity for each of the material points and then take, for example, their harmonic or arithmetic average to compute the bond micro-diffusivity. In this work, the smaller micro-diffusivity is directly used as the micro-diffusivity for the PD bond (see Section 2.2). Note that when diffusivities at the ends of a bond differ by orders of magnitudes, the smaller of the two micro-diffusivities is close to the harmonic average.

The linear profiles for the micro-diffusivity and the micro-velocity lead to a faster convergence rate (convergence of the nonlocal solution to the classical, local solution, in the limit of the horizon going to zero) than the constant ones. Therefore, we use linear profiles for the calculations in this paper.

For the advection part, two basic schemes can be considered: the central scheme and the upwind scheme. In the central scheme, the integral region is the same as the horizon region of x. In the upwind scheme, the integral region is only the "upwind" half of the horizon of x. As shown in [55], the central scheme may lead to instabilities in the

Table 1
The micro-diffusivity and micro-velocity parameters for different horizon-scale behaviors ("constant" and "linear") [55] in terms
of given input data (material diffusivity and velocity).

Function type		Micro-diffusivity parameters	Micro-velocity parameters for the central kernel	Micro-velocity parameters for the upwind kernel
1D	Constant linear	$d_0 = \frac{D}{\delta}$ $d_1 = \frac{2D}{\delta}$	$v_0 = \frac{V}{2\delta}$ $v_1 = \frac{V}{s}$	$ \tilde{v}_0 = \frac{V}{\delta} \\ \tilde{v}_1 = \frac{2V}{\delta} $
2D	Constant	$d_0 = \frac{4D}{\pi \delta^2}$	$\mathbf{v}_0 = \frac{2V}{\pi \delta^2}$	$\tilde{\mathbf{v}}_0 = \frac{4\mathbf{V}}{\pi \delta^2}$
	linear	$d_1 = \frac{12D}{\pi \delta^2}$	$v_1 = \frac{6V}{\pi \delta^2}$	$\tilde{\boldsymbol{v}}_1 = \frac{12\boldsymbol{V}}{\pi\delta^2}$

simulation, and the upwind scheme may lead to numerical diffusion. In this paper, a hybrid scheme is applied [55]:

$$\frac{\partial C\left(\boldsymbol{x},t\right)}{\partial t} = \int_{H_{\mathbf{x}}} d\left(\boldsymbol{x},\boldsymbol{x}',t\right) \frac{C\left(\boldsymbol{x}',t\right) - C\left(\boldsymbol{x},t\right)}{\left\|\boldsymbol{x}' - \boldsymbol{x}\right\|^{2}} dV_{x'} - \omega \int_{H_{\mathbf{x}}} v\left(\boldsymbol{x},\boldsymbol{x}',t\right) \frac{C\left(\boldsymbol{x}',t\right) - C\left(\boldsymbol{x},t\right)}{\left\|\boldsymbol{x}' - \boldsymbol{x}\right\|} dV_{x'} - \omega \int_{H_{\mathbf{x}}} v\left(\boldsymbol{x},\boldsymbol{x}',t\right) \frac{C\left(\boldsymbol{x}',t\right) - C\left(\boldsymbol{x},t\right)}{\left\|\boldsymbol{x}' - \boldsymbol{x}\right\|} dV_{x'} - \omega \int_{H_{\mathbf{x}}} v\left(\boldsymbol{x},\boldsymbol{x}',t\right) \frac{C\left(\boldsymbol{x}',t\right) - C\left(\boldsymbol{x},t\right)}{\left\|\boldsymbol{x}' - \boldsymbol{x}\right\|} dV_{x'} - \omega \int_{H_{\mathbf{x}}} v\left(\boldsymbol{x},\boldsymbol{x}',t\right) \frac{C\left(\boldsymbol{x}',t\right) - C\left(\boldsymbol{x},t\right)}{\left\|\boldsymbol{x}' - \boldsymbol{x}\right\|} dV_{x'} - \omega \int_{H_{\mathbf{x}}} v\left(\boldsymbol{x},\boldsymbol{x}',t\right) \frac{C\left(\boldsymbol{x}',t\right) - C\left(\boldsymbol{x},t\right)}{\left\|\boldsymbol{x}' - \boldsymbol{x}\right\|} dV_{x'} - \omega \int_{H_{\mathbf{x}}} v\left(\boldsymbol{x},\boldsymbol{x}',t\right) \frac{C\left(\boldsymbol{x}',t\right) - C\left(\boldsymbol{x},t\right)}{\left\|\boldsymbol{x}' - \boldsymbol{x}\right\|} dV_{x'} - \omega \int_{H_{\mathbf{x}}} v\left(\boldsymbol{x},\boldsymbol{x}',t\right) \frac{C\left(\boldsymbol{x}',t\right) - C\left(\boldsymbol{x},t\right)}{\left\|\boldsymbol{x}' - \boldsymbol{x}\right\|} dV_{x'} - \omega \int_{H_{\mathbf{x}}} v\left(\boldsymbol{x},\boldsymbol{x}',t\right) \frac{C\left(\boldsymbol{x}',t\right) - C\left(\boldsymbol{x},t\right)}{\left\|\boldsymbol{x}' - \boldsymbol{x}\right\|} dV_{x'} - \omega \int_{H_{\mathbf{x}}} v\left(\boldsymbol{x},\boldsymbol{x}',t\right) \frac{C\left(\boldsymbol{x}',t\right) - C\left(\boldsymbol{x},t\right)}{\left\|\boldsymbol{x} - \boldsymbol{x}\right\|} dV_{x'} - \omega \int_{H_{\mathbf{x}}} v\left(\boldsymbol{x},\boldsymbol{x}',t\right) \frac{C\left(\boldsymbol{x}',t\right) - C\left(\boldsymbol{x},t\right)}{\left\|\boldsymbol{x} - \boldsymbol{x}\right\|} dV_{x'} - \omega \int_{H_{\mathbf{x}}} v\left(\boldsymbol{x},\boldsymbol{x}',t\right) \frac{C\left(\boldsymbol{x}',t\right) - C\left(\boldsymbol{x},t\right)}{\left\|\boldsymbol{x} - \boldsymbol{x}\right\|} dV_{x'} - \omega \int_{H_{\mathbf{x}}} v\left(\boldsymbol{x},\boldsymbol{x}',t\right) \frac{C\left(\boldsymbol{x}',t\right) - C\left(\boldsymbol{x},t\right)}{\left\|\boldsymbol{x} - \boldsymbol{x}\right\|} dV_{x'} - \omega \int_{H_{\mathbf{x}}} v\left(\boldsymbol{x},\boldsymbol{x}',t\right) \frac{C\left(\boldsymbol{x}',t\right) - C\left(\boldsymbol{x},t\right)}{\left\|\boldsymbol{x} - \boldsymbol{x}\right\|} dV_{x'} - \omega \int_{H_{\mathbf{x}}} v\left(\boldsymbol{x},\boldsymbol{x}',t\right) \frac{C\left(\boldsymbol{x}',t\right) - C\left(\boldsymbol{x},t\right)}{\left\|\boldsymbol{x} - \boldsymbol{x}\right\|} dV_{x'} - \omega \int_{H_{\mathbf{x}}} v\left(\boldsymbol{x},\boldsymbol{x}',t\right) \frac{C\left(\boldsymbol{x}',t\right) - C\left(\boldsymbol{x},t\right)}{\left\|\boldsymbol{x} - \boldsymbol{x}\right\|} dV_{x'} - \omega \int_{H_{\mathbf{x}}} v\left(\boldsymbol{x},\boldsymbol{x}',t\right) \frac{C\left(\boldsymbol{x}',t\right) - C\left(\boldsymbol{x},t\right)}{\left\|\boldsymbol{x} - \boldsymbol{x}\right\|} dV_{x'} - \omega \int_{H_{\mathbf{x}}} v\left(\boldsymbol{x},\boldsymbol{x}',t\right) \frac{C\left(\boldsymbol{x},t\right) - C\left(\boldsymbol{x},t\right)}{\left\|\boldsymbol{x} - \boldsymbol{x}\right\|} dV_{x'} - \omega \int_{H_{\mathbf{x}}} v\left(\boldsymbol{x},\boldsymbol{x}',t\right) \frac{C\left(\boldsymbol{x},t\right) - C\left(\boldsymbol{x},t\right)}{\left\|\boldsymbol{x} - \boldsymbol{x}\right\|} dV_{x'} - \omega \int_{H_{\mathbf{x}}} v\left(\boldsymbol{x},\boldsymbol{x}',t\right) \frac{C\left(\boldsymbol{x},t\right) - C\left(\boldsymbol{x},t\right)}{\left\|\boldsymbol{x} - \boldsymbol{x}\right\|} dV_{x'} - \omega \int_{H_{\mathbf{x}}} v\left(\boldsymbol{x},\boldsymbol{x}',t\right) \frac{C\left(\boldsymbol{x},t\right) - C\left(\boldsymbol{x},t\right)}{\left\|\boldsymbol{x} - \boldsymbol{x}\right\|} dV_{x'} - \omega \int_{H_{\mathbf{x}}} v\left(\boldsymbol{x},\boldsymbol{x}',t\right) \frac{C\left(\boldsymbol{x},t\right) - C\left(\boldsymbol{x},t\right)}{\left\|\boldsymbol{x} - \boldsymbol{x}\right\|} dV_{x'} - \omega \int_{H_{\mathbf{x}}} v\left(\boldsymbol{x},\boldsymbol{x}',t\right) \frac$$

$$(1 - \omega) \int_{\tilde{H}_{x}} \tilde{v}\left(\mathbf{x}, \mathbf{x}', t\right) \frac{C\left(\mathbf{x}', t\right) - C\left(\mathbf{x}, t\right)}{\|\mathbf{x}' - \mathbf{x}\|} dV_{x'} + R\left(\mathbf{x}, t\right), \tag{4}$$

where  $\tilde{v}(x, x', t)$  is the micro-velocity for the upwind kernel. For all the PD calculations in this paper, we apply the hybrid scheme. The hybrid formulation could suffer from both the instabilities in the simulation and the numerical diffusion. Selecting a proper hybrid weight  $(\omega)$  can lessen these two issues simultaneously. The optimal value of  $\omega$  in the hybrid scheme is related to the Peclet number, Pe =  $\frac{VL}{D}$ , (see [61]), meaning that for different Peclet number, different  $\omega$  should be used. According to the results shown in [55], when v = 0.0121 cm/s, d = 0.0017 cm<sup>2</sup>/s, for an advection-diffusion process in a 30 cm-length region,  $\omega = 0.8$  is the optimal hybrid weight for stable and accurate PD solution. In this work, we applied the similar velocity and diffusion values for most of the 2D simulations. Therefore, we fixed the hybrid weight to be 0.8.

Eq. (1) describes an advection-diffusion process in a domain. Suppose in the domain a series of chemical reactions (or other types of reactions, e.g. nuclear) are also taking place. The species concentration at a point changes also because of these reactions and needs to be considered when solving for its evolution. Consider  $N_s$  species, with concentrations  $C_i$ , where  $i = 1, 2, ..., N_s$ . The *i*th species is involved in  $M_i$  reactions with other species. Note that the *i*th species can be a reactant or a product. The governing equation for the concentration of species *i* is:

$$\frac{\partial C_{i}(\mathbf{x},t)}{\partial t} = \int_{H_{\mathbf{x}}} d(\mathbf{x}, \mathbf{x}', t) \frac{C_{i}(\mathbf{x}', t) - C_{i}(\mathbf{x}, t)}{\|\mathbf{x}' - \mathbf{x}\|^{2}} dV_{\mathbf{x}'} - \int_{H_{\mathbf{x}}} v(\mathbf{x}, \mathbf{x}', t) \frac{C_{i}(\mathbf{x}', t) - C_{i}(\mathbf{x}, t)}{\|\mathbf{x}' - \mathbf{x}\|} dV_{\mathbf{x}'} + \sum_{i=1}^{M_{i}} R_{ij}(\mathbf{x}, t),$$
(5)

where  $R_{ij}(x, t)$  is the jth  $(j \in [1, M_i])$  reaction term. According to the role (reactant or product) of a species in the reaction,  $R_{ij}(x, t)$  can be a negative or positive function. Since  $R_{ij}(x, t)$  is usually a function of the concentrations of all species, we have to solve a coupled system of integro-differential equations (Eq. (5)) to obtain  $C_i(x, t)$ .

In Eq. (5), the reaction terms can be identical to those used in the classical, local equations. Two reasons can be found for adopting this form: (1) the local collision of molecules is essential in chemical reactions; (2) there are no spatial derivatives in the reaction terms, eliminating the need for replacing them with integral operators in order to maintain the strength of the model when dealing with spatial discontinuities. Nonlocality in the PD reaction–diffusion model in Eq. (5) is present in the flow and diffusion terms. Nonlocality could be used in the reaction terms if homogenization is intended to be used while preserving some small-scale properties and their influence on the larger scale (see, e.g. [30,62]). Note that  $R_{ij}(x,t)$  takes different forms according to the reaction type. In the following subsections, we discuss two types of reactions and the formulas for the corresponding reaction terms.

### 2.1. PD equations for advection-diffusion-and-bimolecular-reaction

In this section, we consider three substances (A, B, and AB) involved in an irreversible bimolecular synthesis reaction:  $A + B \rightarrow AB$ . These molecular species are solutes dissolved in the solvent, water. Species A and B react to form species AB, and the solvent flows through a tube (1D problem). Therefore, to model the evolution of the substances, we need to consider the diffusion of all three substances in water, the water flow, and the reaction. The classical governing equations for this 1D ARD problem are [56]:

$$\begin{cases}
\frac{\partial C_{A}(x,t)}{\partial t} = D \frac{\partial^{2} C_{A}(x,t)}{\partial x^{2}} - V \frac{\partial C_{A}(x,t)}{\partial x} - R_{AB} C_{A}(x,t) C_{B}(x,t) \\
\frac{\partial C_{B}(x,t)}{\partial t} = D \frac{\partial^{2} C_{B}(x,t)}{\partial x^{2}} - V \frac{\partial C_{B}(x,t)}{\partial x} - R_{AB} C_{A}(x,t) C_{B}(x,t) \\
\frac{\partial C_{AB}(x,t)}{\partial t} = D \frac{\partial^{2} C_{AB}(x,t)}{\partial x^{2}} - V \frac{\partial C_{AB}(x,t)}{\partial x} + R_{AB} C_{A}(x,t) C_{B}(x,t)
\end{cases} , \tag{6}$$

where  $C_A$ ,  $C_B$ ,  $C_{AB}$  are the concentrations of A, B, and AB, respectively; D is the diffusion coefficient; V is the constant velocity of the flow field;  $R_{AB}$  is the reaction coefficient for the bimolecular synthesis reaction. This model assumes that all substances have the same diffusion coefficient. Different diffusion coefficients can easily be considered for cases in which the species diffuse at different rates in the solvent. Referring to Eq. (5), Eq. (6) can be written as:

$$\begin{cases}
\frac{\partial C_{A}(x,t)}{\partial t} = \int_{H_{x}} d\left(x,x',t\right) \frac{C_{A}(x,t) - C_{A}(x',t)}{|x'-x|^{2}} dV_{x'} - \\
\int_{H_{x}} v\left(x,x',t\right) \frac{C_{A}(x,t) - C_{A}(x',t)}{|x'-x|} dV_{x'} - R_{AB}C_{A}(x,t) C_{B}(x,t) \\
\frac{\partial C_{B}(x,t)}{\partial t} = \int_{H_{x}} d\left(x,x',t\right) \frac{C_{B}(x,t) - C_{B}(x',t)}{|x'-x|^{2}} dV_{x'} - \\
\int_{H_{x}} v\left(x,x',t\right) \frac{C_{B}(x,t) - C_{B}(x',t)}{|x'-x|} dV_{x'} - R_{AB}C_{A}(x,t) C_{B}(x,t) \\
\frac{\partial C_{AB}(x,t)}{\partial t} = \int_{H_{x}} d\left(x,x',t\right) \frac{C_{AB}(x,t) - C_{AB}(x',t)}{|x'-x|^{2}} dV_{x'} - \\
\int_{H_{x}} v\left(x,x',t\right) \frac{C_{AB}(x,t) - C_{AB}(x',t)}{|x'-x|} dV_{x'} + R_{AB}C_{A}(x,t) C_{B}(x,t)
\end{cases} (7)$$

These are three coupled integro-differential equations for three unknown functions,  $C_A$ ,  $C_B$ , and  $C_{AB}$ . With given initial and boundary conditions, the system can be solved numerically. The numerical discretization and computational method are explained in Section 3, and examples (including both 1D and 2D cases) are shown in Sections 4.1 and 4.2. The formulation for the 2D case is given in Section 4.2.

# 2.2. PD equation of hydrolysis reaction-diffusion problem

The reaction term (reaction rate) for the bimolecular synthesis reaction depends linearly on the reactants' concentrations, as shown in the last section. For some reactions, this dependence could be more complicated. For instance, the reaction rate of hydrolysis reaction ( $M \rightarrow \alpha m$ , a solid-state polymer changes to dissolvable monomers) follows pseudo-first-order kinetics [63], and a stochastic hydrolysis model [64] is applied to represent this reaction process. This section introduces a PD model for the hydrolysis reaction, a typical form of polymer degradation process. The model can be applied to the degradation of polymeric biomaterials, simulating biodegradable implants, and drug delivery systems.

The flow of hydrolytic monomers is ignored here. The reaction-diffusion equation for hydrolytic monomers can be written as:

$$\frac{\partial C_{\mathrm{m}}\left(\boldsymbol{x},\ t\right)}{\partial t} = \int_{H_{x}} d_{\mathrm{m}}\left(\boldsymbol{x},\boldsymbol{x}',t\right) \frac{C_{\mathrm{m}}\left(\boldsymbol{x}',\ t\right) - C_{\mathrm{m}}\left(\boldsymbol{x},t\right)}{\left\|\boldsymbol{x}'-\boldsymbol{x}\right\|^{2}} dV_{x'} + R\left(\boldsymbol{x},t\right),\tag{8}$$

where R(x,t) is the reaction term, the reaction rate at which the hydrolytic monomers are released from the hydrolysis reaction, while  $d_m(x,x',t)$  is the micro-diffusivity function of hydrolyzate. The micro-diffusivity can have different forms and the most common ones are the constant form and the linear form. Exponential ones are also common but more expensive to compute. The 2D linear form is applied in this paper for a faster convergence to classical solutions (see discussion on this topic in [3,44]):

$$d_{\mathrm{m}}\left(\mathbf{x}, \mathbf{x}', t\right) = \frac{12D_{\mathrm{m}}}{\pi \delta^{2}} \left(1 - \frac{\|\mathbf{x}' - \mathbf{x}\|}{\delta}\right),\tag{9}$$

 $D_m$  approximately expressed as an exponential function [64]:

$$D_{\rm m} = D_{\rm m}^0 e^{S_{\rm m}(1-\gamma)},\tag{10}$$

where  $S_m$  is a constant related to the polymer material,  $D_m^0$  represents the measured diffusivity of hydrolyzate in the corresponding polymer matrix, and  $\gamma$ , a function of time and position, indicates the hydrolytic state of the polymer.  $\gamma=1$  represents the state of the polymer without hydrolysis,  $\gamma=0.001$  represents the state of a monomer that has been hydrolyzed, and  $\gamma=0$  represents the state of water [64]. Note that the ends of the bond (x,x') may locate at material points with different hydrolytic states. In this case, the smaller micro-diffusivity is directly used as the micro-diffusivity for the PD bond.

R(x, t), the source term of hydrolyzed monomer, is determined by the hydrolysis, and the conditions are as follows [64]:

$$R(x,t) = \begin{cases} 0, & P_{R} \ge P_{H} \\ R_{0}, & P_{R} < P_{H}, \end{cases} P_{H} = \frac{\lambda_{0}e^{-\lambda_{0}t}\left(1 + \beta\left(e^{C_{m}-1}\right)\right)}{F_{0}F(t)}, 0 < P_{R} < 1,$$

$$(11)$$

where  $R_0$  is the value of the source term when hydrolysis occurs,  $P_H$  is a hydrolytic probability function considering the autocatalytic effect,  $\lambda_0$  is the degradation rate constant, and  $\beta$  is a constant that represents the strength of the autocatalytic effect.  $F_0$  and F(t) represent the initial volume fraction of the polymer and the volume fraction at time t, respectively.  $P_R$  is a random number, generated in between 0 and 1 from a uniform probability distribution function. If  $P_R$  is less than  $P_H$ , the hydrolysis occurs, meaning that the polymer at that material point converts into a certain concentration of hydrolyzed monomer.

# 3. Numerical discretization

Although some PD equations set in simple domains can be solved analytically [21,65,66], for the rest we have to employ numerical approximation schemes. To numerically discretize Eq. (5), we use the mid-point (or one-point Gaussian) quadrature scheme for the integral operators. We generate a uniform grid with grid spacing  $\Delta x$  (see Fig. 2) to discretize the domain. Each node has a "volume" (length in 1D and area in 2D). Fig. 2 shows the 2D discretization around a node at  $x_p$ ,  $x_j$  is any point within the horizon of  $x_p$ ,  $e_{pj}$  is the direction vector of the  $(x_p, x_j)$  bond,  $\alpha$  is the angle between  $e_{pj}$  and the flow direction.

Eq. (5) can be spatially discretized with the mid-point algorithm as follows:

$$\frac{\partial C_{i}\left(\boldsymbol{x}_{p},t\right)}{\partial t} = \sum_{q} d\left(\boldsymbol{x}_{p},\boldsymbol{x}_{q},t\right) \frac{C_{i}\left(\boldsymbol{x}_{q},t\right) - C_{i}\left(\boldsymbol{x}_{p},t\right)}{\left\|\boldsymbol{x}_{q} - \boldsymbol{x}_{p}\right\|^{2}} V_{pq} - \sum_{l} v\left(\boldsymbol{x}_{p},\boldsymbol{x}_{l},t\right) \frac{C_{i}\left(\boldsymbol{x}_{l},t\right) - C_{i}\left(\boldsymbol{x}_{p},t\right)}{\left\|\boldsymbol{x}_{l} - \boldsymbol{x}_{p}\right\|} V_{pl} + \sum_{j}^{M_{i}} R_{ij}\left(\boldsymbol{x}_{p},t\right)$$

$$= \sum_{q} Q_{d,pq} - \sum_{l} Q_{v,Pl} + \sum_{j}^{M_{i}} R_{ij}\left(\boldsymbol{x}_{p},t\right)$$
(12)

where,

$$Q_{d,pq} = d\left(\mathbf{x}_{p}, \mathbf{x}_{q}, t\right) \frac{C_{i}\left(\mathbf{x}_{q}, t\right) - C_{i}\left(\mathbf{x}_{p}, t\right)}{\left\|\mathbf{x}_{q} - \mathbf{x}_{p}\right\|^{2}} V_{pq}, \tag{13}$$

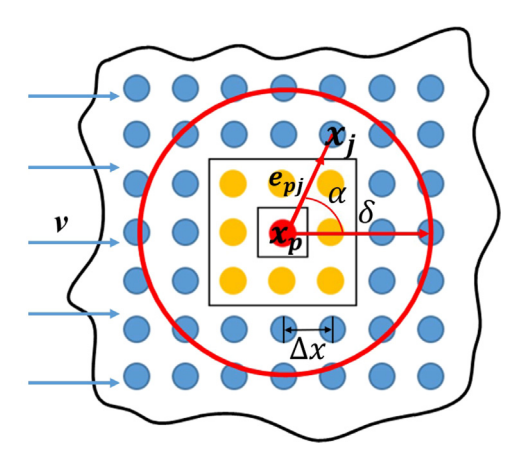


Fig. 2. Numerical discretization around node  $x_p$  [55]. The circular region is the horizon region of  $x_p$ . The ARD in its own volume (small square) includes the nearest-neighbor nodes of the node  $x_p$ .

$$Q_{v,pl} = v\left(\mathbf{x}_{p}, \mathbf{x}_{l}, t\right) \frac{C_{i}\left(\mathbf{x}_{l}, t\right) - C_{i}\left(\mathbf{x}_{p}, t\right)}{\|\mathbf{x}_{l} - \mathbf{x}_{p}\|} V_{pl}, \tag{14}$$

In Eq. (12), the first two summations include all nodes  $x_q$  or  $x_l$  inside the horizon of node  $x_p$ , and  $V_{pq}$  ( $V_{pl}$ ) is the portion of the volume of node  $x_q$  ( $x_l$ ) covered by the horizon of node  $x_p$ . The HHB algorithm [23,67] for the partial volume integration is used to approximate the covered portion of  $V_{pq}$  and  $V_{pl}$ . Note that the second summation, corresponding to the advection terms, differs between the central and upwind schemes. Only those nodes located in the upwind region are included in the upwind scheme.

Special care should be taken when computing the term for q = p or l = p. Mathematically, this term can be computed by taking the limit  $x_q \to x_p$  or  $x_l \to x_p$ , but note that this implies that the corresponding volumes of these nodes tend to zero, otherwise, it violates the principle of non-interpenetration of matter. Instead of the limit approach for these values, we approximate them by the average value from the nearest neighbors [44].

For the diffusion term in 1D,

$$Q_{d,pp} = \frac{1}{2} \left[ d\left(x_{p-1}, x_{p}\right) \frac{C\left(x_{p-1}, t\right) - C\left(x_{p}, t\right)}{\left(x_{p-1} - x_{p}\right)^{2}} V_{p,p-1} + d\left(x_{p+1}, x_{p}\right) \frac{C\left(x_{p+1}, t\right) - C\left(x_{p}, t\right)}{\left(x_{p+1} - x_{p}\right)^{2}} V_{p,p+1} \right],$$
(15)

in 2D,

$$Q_{d,pp} = \frac{1}{8} \sum_{j=1}^{8} d(\mathbf{x}_{j}, \mathbf{x}_{p}) \frac{C(\mathbf{x}_{j}, t) - C(\mathbf{x}_{p}, t)}{\|\mathbf{x}_{j} - \mathbf{x}_{p}\|^{2}} V_{pj},$$
(16)

for the advection term, different integration schemes should to be considered. For the central scheme in 1D,

$$Q_{v,pp} = \frac{1}{2} \left[ v\left(x_{p-1}, x_p\right) \frac{C\left(x_{p-1}, t\right) - C\left(x_p, t\right)}{x_{p-1} - x_p} V_{p,p-1} + v\left(x_{p+1}, x_p\right) \frac{C\left(x_{p+1}, t\right) - C\left(x_p, t\right)}{x_{p+1} - x_p} V_{p,p+1} \right], (17)$$

while for the upwind scheme in 1D,

$$Q_{v,pp} = \frac{1}{2} \left[ \tilde{v} \left( x_{p-1}, x_p \right) \frac{C \left( x_{p-1}, t \right) - C \left( x_p, t \right)}{x_{p-1} - x_p} V_{p,p-1} \right], \tag{18}$$

In Eq. (18), we consider the flow direction is from left to right. If the flow direction is from right to left, the  $x_{p-1}$  in the third term of Eq. (18) should be replaced by  $x_{p+1}$ . In a body that undergoes damage, if one of the mechanical bonds  $(x_{p-1}, x_p)$  or  $(x_p, x_{p+1})$  gets broken and the advection or diffusion interrupts, then the term of q = p is computed to be the same as the term of q = p - 1 or q = p + 1.

For the 2D case with the central scheme, we have

$$Q_{v,pp} = \frac{1}{8} \sum_{i=1}^{8} v\left(\boldsymbol{x}_{j}, \boldsymbol{x}_{p}\right) \frac{C\left(\boldsymbol{x}_{j}, t\right) - C\left(\boldsymbol{x}_{p}, t\right)}{\left\|\boldsymbol{x}_{j} - \boldsymbol{x}_{p}\right\|} \cos\left(\alpha\right) V_{pj},\tag{19}$$

where  $\alpha$  is the angle between PD bond and flow velocity  $\nu$ . For the upwind scheme,

$$Q_{v,pp} = \frac{1}{3} \sum_{i=1}^{3} \tilde{v}\left(\boldsymbol{x}_{j}, \boldsymbol{x}_{p}\right) \frac{C\left(\boldsymbol{x}_{j}, t\right) - C\left(\boldsymbol{x}_{p}, t\right)}{\left\|\boldsymbol{x}_{j} - \boldsymbol{x}_{p}\right\|} \cos\left(\alpha\right) V_{pj}. \tag{20}$$

This discretization method can be easily extended to the 3D case.

For time integration we use the forward Euler's method:

$$C_p^{n+1} = C_p^n + \Delta t \dot{C}_p^n, \tag{21}$$

where  $C_p^n$  represents the concentration at nodal point  $x_p$  and the *n*th time step,  $\Delta t$  is the time step, and the dot on the top of  $C_p^n$  means the time derivative. Euler's method has first-order accuracy, and it is conditionally stable. To analyze the computational stability, we first ignore the inhomogeneous term (the reaction term) in Eq. (12), leading to:

$$\frac{\partial C_i\left(\boldsymbol{x}_{\boldsymbol{p}},t\right)}{\partial t} = \sum_{\boldsymbol{q}} d\left(\boldsymbol{x}_{\boldsymbol{p}},\boldsymbol{x}_{\boldsymbol{q}},t\right) \frac{C_i\left(\boldsymbol{x}_{\boldsymbol{q}},t\right) - C_i\left(\boldsymbol{x}_{\boldsymbol{p}},t\right)}{\left\|\boldsymbol{x}_{\boldsymbol{q}} - \boldsymbol{x}_{\boldsymbol{p}}\right\|^2} V_{pq} - \sum_{l} v\left(\boldsymbol{x}_{\boldsymbol{p}},\boldsymbol{x}_{l},t\right) \frac{C_i\left(\boldsymbol{x}_{\boldsymbol{l}},t\right) - C_i\left(\boldsymbol{x}_{\boldsymbol{p}},t\right)}{\left\|\boldsymbol{x}_{\boldsymbol{l}} - \boldsymbol{x}_{\boldsymbol{p}}\right\|} V_{pl}. \tag{22}$$

In the following, we derive the stability condition for applying the forward Euler's method to numerically solve Eq. (22) considering both diffusion and advection terms. We use the von Neumann stability analysis [27]. Let:

$$\varepsilon_n^n = \zeta^n e^{i\kappa p},\tag{23}$$

be the solution error for Eq. (21) at nodal point p and the nth time step, where  $\kappa$  is a positive value, and  $\zeta$  is a complex value. Note that from Eq. (23) to Eq. (33),  $i = \sqrt{-1}$  is the imaginary unit. The allowable  $\Delta t$  is found by requiring that  $\|\zeta\| \le 1$  for any  $\kappa$ .  $\varepsilon_p^n$  should also satisfy Eqs. (21) and (22). Substituting Eq. (23) into Eq. (22), we have:

$$\frac{\zeta - 1}{\Delta t} = \sum_{q} \frac{d}{\|\mathbf{x}_{q} - \mathbf{x}_{p}\|^{2}} \left( e^{i\kappa(q - p)} - 1 \right) V_{pq} - \sum_{l} \frac{v}{\|\mathbf{x}_{l} - \mathbf{x}_{p}\|} \left( e^{i\kappa(l - p)} - 1 \right) V_{pl}, \tag{24}$$

Then

$$\|\boldsymbol{\zeta}\| = \left\| 1 + \Delta t \left( \sum_{q} \frac{d}{\|\boldsymbol{x}_{q} - \boldsymbol{x}_{p}\|^{2}} \left( e^{i\kappa(q-p)} - 1 \right) V_{pq} - \sum_{l} \frac{v}{\|\boldsymbol{x}_{l} - \boldsymbol{x}_{p}\|} \left( e^{i\kappa(l-p)} - 1 \right) V_{pl} \right) \right\| \le 1, \tag{25}$$

where.

$$e^{ix} = \cos x - i\sin x. \tag{26}$$

For the central scheme, Eq. (25) can be written as (the summation of the terms containing the sine function is zero):

$$\|\xi\| = \left\| 1 + \Delta t \sum_{q} \left( \frac{v}{\|x_q - x_p\|} - \frac{d}{\|x_q - x_p\|^2} \right) (1 - \cos \kappa (q - p)) V_{pq} \right\| \le 1.$$
 (27)

The inequality in Eq. (27) leads to:

$$-2 \le \Delta t \sum_{q} \left( \frac{v}{\|x_{q} - x_{p}\|} - \frac{d}{\|x_{q} - x_{p}\|^{2}} \right) (1 - \cos \kappa (q - p)) V_{pq} \le 0.$$
 (28)

The no-more-than-zero condition cannot be satisfied if  $d < v \|x_q - x_p\|$  for all PD bonds. We assume that  $d \ge v \|x_q - x_p\|$ . Eq. (24) can be written as:

$$\Delta t \le \frac{2}{\sum_{q} \left( \frac{d}{\|x_{q} - x_{p}\|^{2}} - \frac{v}{\|x_{q} - x_{p}\|} \right) (1 - \cos \kappa (q - p)) V_{pq}}.$$
 (29)

Since  $|1 - \cos \kappa (q - p)| \le 2$ , to satisfy Eq. (29) is sufficient to have:

$$\Delta t \le \frac{1}{\sum_{q} \left( \frac{d}{\|x_{q} - x_{p}\|^{2}} - \frac{v}{\|x_{q} - x_{p}\|} \right) V_{pq}}.$$
(30)

Therefore, Eq. (30) and  $d \ge v \|x_q - x_p\|$  are a set of sufficient conditions for applying the central scheme with the forward Euler's method to solve Eq. (22).

For the upwind scheme, Eq. (25) can be written as:

$$\|\xi\| = \left\| 1 + \Delta t \sum_{q} \left( \frac{0.5v}{\|x_{q} - x_{p}\|} - \frac{d}{\|x_{q} - x_{p}\|^{2}} \right) (1 - \cos \kappa (q - p)) V_{pq} + \Delta t \sum_{l} \frac{v}{\|x_{l} - x_{p}\|} (i \sin \kappa (l - p)) V_{pl} \right\| \le 1.$$
(31)

Note that in the second summation term, only the family nodes (the points included in the horizon) in the upwind region are considered. Since  $|1 - \cos \kappa (q - p)| \le 2$  and  $||i \sin \kappa (l - p)|| \le 1$ , we have:

$$\left\| 1 + \Delta t \sum_{q} \left( \frac{0.5v}{\|x_{q} - x_{p}\|} - \frac{d}{\|x_{q} - x_{p}\|^{2}} \right) (1 - \cos \kappa (q - p)) V_{pq} + \Delta t \sum_{l} \frac{v}{\|x_{l} - x_{p}\|} (i \sin \kappa (l - p)) V_{pl} \right\| \\
\leq \left\| 1 + \Delta t \sum_{q} 2 \left( \frac{0.5v}{\|x_{q} - x_{p}\|} - \frac{d}{\|x_{q} - x_{p}\|^{2}} \right) V_{pq} + \Delta t \sum_{l} \frac{v}{\|x_{l} - x_{p}\|} V_{pl} \right\| \\
\leq \left\| 1 + \Delta t \sum_{q} \left( 2 \left( \frac{0.5v}{\|x_{q} - x_{p}\|} - \frac{d}{\|x_{q} - x_{p}\|^{2}} \right) + \frac{0.5v}{\|x_{p} - x_{p}\|} \right) V_{pq} \right\| \\
= \left\| 1 + \Delta t \sum_{q} \left( \frac{1.5v}{\|x_{q} - x_{p}\|} - \frac{2d}{\|x_{q} - x_{p}\|^{2}} \right) V_{pq} \right\| \leq 1, \tag{32}$$

Therefore, we obtain a set of sufficient conditions for applying the upwind scheme with the forward Euler's method to solve Eq. (22):  $d \ge 0.75v \|x_q - x_p\|$ , and,

$$\Delta t \le \frac{1}{\sum_{q} \left( \frac{d}{\|x_{q} - x_{p}\|^{2}} - \frac{0.75v}{\|x_{q} - x_{p}\|} \right) V_{pq}},\tag{33}$$

Obviously, the sufficient conditions for the central scheme are also sufficient conditions for the upwind scheme, which is consistent with the conclusion in Ref. [55]: the central scheme is more likely to lead to numerical instabilities. Note that the stability condition given in [55] only considered the diffusion term, while in this work, the stability conditions are obtained considering diffusion and advection terms, concurrently.

Note that it is difficult to directly compare the stability conditions between Euler's method for PD and for the corresponding PDE, because of the length-scale introduced by the horizon size in PD, in addition to the grid spacing used for the discretization. The conditions given in Eqs. (29) and (33) are sufficient conditions which depend on the horizon size (summations of grid spacings over the horizon region). For convergence of analytical solutions of transient diffusion PD models to corresponding classical ones, please see [66]. Comparing stability conditions between discretizations of PD models and their corresponding PDE-based discretizations has been recently studied in [68] for transient diffusion. Similar developments for ARD problems are planned for the future.

The stability conditions for using Euler's method to solve Eq. (12) also depend on the relationship between  $R_{ij}(x_p,t)$  and  $C_i(x_p,t)$ . For a fixed time step, if the reaction rate is large enough, within one time step of calculation, the reactant concentration could drop to below zero which is unphysical. To avoid this numerical situation, a sufficient condition is: for all reactants (for which the reaction rates are negative, see Eq. (7)) we enforce the following inequality:  $-\Delta t \sum_{j}^{M_i} R_{ij}(x_p,t) \leq C_i(x_p,t)$ . This condition prevents ending up with negative concentrations at a particular time-step. For example, in the bimolecular reaction considered in Section 2.1, we impose  $\Delta t \leq \frac{1}{R_{AB}C_A}$  and  $\Delta t \leq \frac{1}{R_{AB}C_B}$ . By substituting the reaction coefficient, and the initial maximum concentration for the reactants A and B, we can estimate a maximum value for  $\Delta t$ . However,  $R_{ij}(x_p,t)$  could

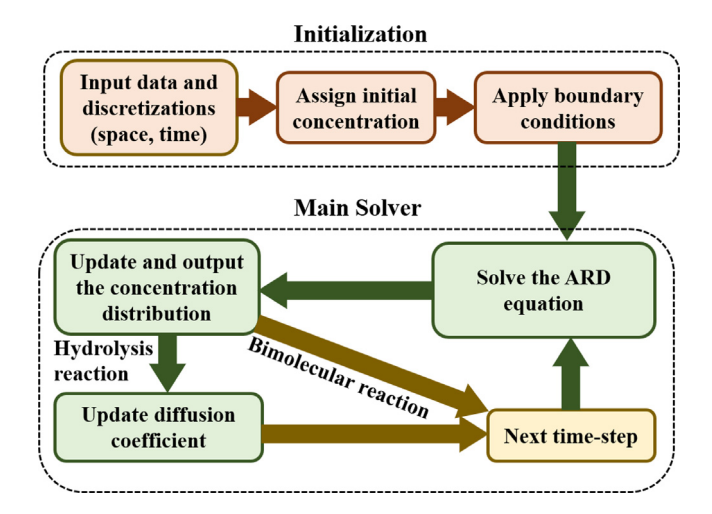


Fig. 3. Graphical illustration of the peridynamic ARD solver for hydrolysis and bimolecular reactions. See Appendix A for details of the numerical implementation.

have a much more complex form (see Section 2.2). In such cases, a convergence study in terms of  $\Delta t$  going to zero, starting from the value given by Eq. (30), can be used.

For the uniform discretization mentioned at the beginning of this section, the Dirichlet boundary conditions can be imposed by assigning the given concentration to the end node/nodes, which is the so-called inner-type method. Another type of method, "fictitious nodes methods (FNM)" [21,69], is adding a boundary layer (with a thickness of  $\delta$ ) outside the real boundary. On the boundary layer, the concentration field is either related by mirror symmetry to the corresponding domain in the deformable body (mirror-type), or constant and equal to the value of the local Dirichlet condition (naïve-type). Both inner-type and fictitious nodes methods show little difference when m (horizon factor, the ratio between the horizon size and the grid spacing) is not large, and node spacing is relatively small, but when m is larger than 4, the FNM gives more accurate results (if we set the classical solutions as the reference) [3]. With the horizon size approaching zero (in a  $\delta$ -convergence study, which induces the nodal volumes to go to zero in concert with the horizon size), the PD Dirichlet condition converges to the classical boundary condition.

The computation time for PD simulation mainly include the computer time for the family search (the search for the points included in the horizon region) and for the iteration of the PD dynamic solver. The computer times for both the family search and the iteration of the PD dynamic solver depend on the total nodal number and the horizon factor (m, the ratio between the horizon size and the grid spacing, which determines the number of nodes inside a full horizon region). The computer time for the family search is usually longer than one iteration of the PD dynamic solver. For a 2D ARD model with m = 4 and 10,000 nodes, with an Intel(R) Core(TM) i7-7700K CPU (4.20 GHz), it takes 137.7 s computer time to calculate 10,000 steps (including the family search time), while the family search itself takes 4.3 s computer time.

Compared to the work in [55], we provide a new nonlocal platform for ARD problems, and a new way of treating multiple reactions, as coupled equations (note that in [55,70], reactions were not considered); we also provide new numerical algorithms for solving these coupled integral—differential equations. Fig. 3 and Appendix A shows the calculation flow for the peridynamic ARD solver for the model in Eq. (5) for certain boundary and initial conditions. In the next section, we apply this calculation to several tests to verify the new PD-ARD model.

# 4. Numerical examples

In this section, a 1D ARD example with bimolecular reaction  $(A + B \rightarrow AB)$  is simulated with the PD model introduced in the previous sections. The numerical results are compared with experimental data and analytical solutions of the corresponding classical model. In this case, the reaction rate is assumed to be very large, in order to obtain the analytical solution for the classical model, meaning that molecules A and B react instantly and completely once they encounter each other. After validation of the 1D model, some parametrical studies are performed to reveal

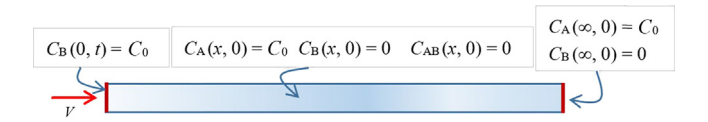


Fig. 4. Initial and boundary conditions for a 1D ARD process in a semi-infinite tube.

the quantitative effects of advection, reaction, and diffusion. Then, with the same type of reaction as in the 1D case, the model is applied to simulate ARD in 2D domains, in both homogeneous and heterogeneous media. In the last subsection, the model is used to simulate polymer implant degradation induced by the hydrolysis reaction, with a stochastic hydrolysis model. Note that to implement boundary conditions in PD models, a fictitious boundary layer with thickness  $\delta$  is added to the actual boundary to eliminate the surface effect [71].

### 4.1. A 1D bimolecular reaction problem

For 1D ARD problems with bimolecular reaction  $(A + B \rightarrow AB)$  described in Eq. (6), we consider a case with initial and boundary conditions shown in Fig. 4:

$$\begin{cases} C_{A}(x,0) = C_{0} & x \ge 0 \\ C_{B}(x,0) = 0 & x > 0 \end{cases}$$

$$\begin{cases} C_{AB}(x,0) = 0 & x \ge 0 \\ C_{AB}(x,0) = 0 & t \ge 0 \end{cases}$$

$$\begin{cases} C_{B}(0,t) = C_{0} & t \ge 0 \\ C_{B}(\infty,0) = 0 & t \ge 0 \end{cases}$$

$$(34)$$

where  $C_0 = 0.02$  mol/L, is applied for the tests shown in this subsection and Section 4.2.

The case shown in Fig. 4 was studied analytically and experimentally in [56]. The analytical solution of the concentration  $C_{A+AB}$  (the sum of concentrations of A and AB) evolution for the 1D case shown in Fig. 4 can be obtained via Standard Pore-Scale Mixed (SPSM) method as [56]:

$$\frac{C_{\text{A+AB}}}{C_0} = \frac{1}{2} \operatorname{erfc}\left(\frac{x - Vt}{2\sqrt{Dt}}\right) + \sqrt{\frac{V^2t}{\pi D}} \exp\left[-\frac{(x - Vt)^2}{4Dt}\right] - \frac{1}{2}\left(1 + \frac{Vx}{D} + \frac{V^2t}{D}\right) \exp\left(\frac{Vx}{D}\right) \operatorname{erfc}\left(\frac{x + Vt}{2\sqrt{Dt}}\right),\tag{35}$$

where erfc  $(x) = \frac{2}{\sqrt{\pi}} \int_{x}^{\infty} e^{-\eta^2} d\eta$  is the complementary error function. When the value of D is much smaller than Vx, the solution can be approximately expressed as:

$$\frac{C_{\text{A+AB}}}{C_0} = \frac{1}{2} \operatorname{erfc}\left(\frac{x - Vt}{2\sqrt{Dt}}\right),\tag{36}$$

and for the case we simulated, the difference between the results calculated by Eqs. (35) and (36) is less than 1.5%. From Eq. (36) we find [56]:

$$\frac{C_{\text{AB}}}{C_0} = \frac{1}{2} \text{erfc} \left( \frac{|x - Vt|}{2\sqrt{Dt}} \right). \tag{37}$$

In a 1D experiment shown in [56], the diffusion coefficient  $D = 0.0017 \text{ cm}^2/\text{s}$ , the flow velocity V = 0.0121 cm/s. The focus, in the literature [56] and in our paper, is on behavior at the centimeter scale. At this scale, D is much smaller than Vx, and the reaction rate is also sufficiently large, meaning that Eq. (37) is a valid approximation of the solution to Eqs. (6) and (34). Note that the approximate analytical solution is for a process in a semi-infinite tube, while in the PD model simulation, the tube length L is finite with L = 30 cm.

The PD solution, approximate analytical solution, and the experimental data [8,56] of the product species (AB) distribution at t = 916 s are shown in Fig. 5. For the PD simulations, the reaction rate  $R_{AB} = 4.1$  L/(mol s) is applied. The results shown from the PD model were obtained using a horizon size  $\delta = 0.5$  cm (see Appendix B

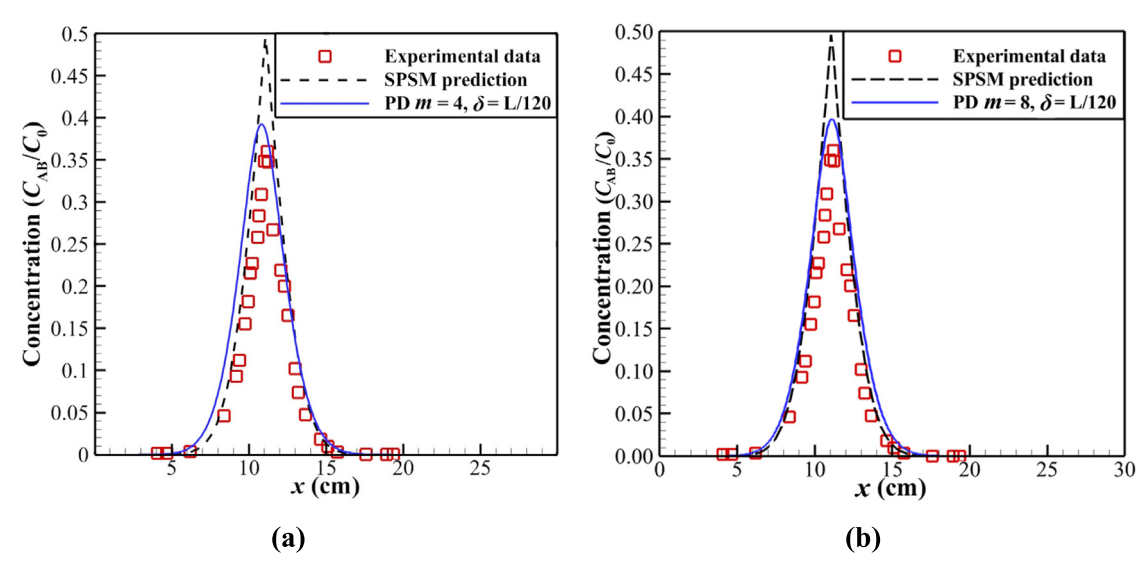


Fig. 5. Comparison between the SPSM prediction, experimental data [56] and PD solution for the 1D example at t = 916 s: (a) m = 4,  $\delta = L/120$ ; (b) m = 8,  $\delta = L/120$ . We use iteration time step  $\Delta t = 0.01$  s for all 1D cases.

for a convergence study) and m=4 (Fig. 5(a), m is the ratio between the horizon size and the grid spacing) or m=8 (Fig. 5(b)). Fig. 5 shows that the PD solution quantitatively matches the experimental measurements in terms of both the profile and peak location. The peak value of the product concentration obtained from the PD model is closer to the experimental data than the approximate analytical value of the corresponding classical model, since the classical model assumes that molecules A and B react instantly and completely once they encounter each other, while this assumption is not valid in experiments, and is not used in the PD model. The peak value from the approximate analytical solution is higher than the other two because the analytical solution assumes an infinite reaction rate. As expected, when the reaction rate decreases, the peak value obtained from the PD simulation also decreases (see Fig. 6(a)). The comparison shown in Fig. 5 indicates that the PD model can be used to simulate and predict the ARD processes. Although m=8 leads to higher computational accuracy, in seeking of a higher computational efficiency, we select m=4 for the rest of the 1D and 2D calculations. The accuracy for the case with m=4 is acceptable for engineering applications, as shown in Fig. 5 and Appendix B. Therefore, in the following calculations for the 1D case, we use m=4,  $\delta=L/120$  and the grid spacing  $\Delta x=\delta/m=L/480$ .

To further verify our PD model, we next perform a parametric study to investigate the effect of D, V, and  $R_{\rm AB}$  parameters on the evolution of the product AB, respectively. We monitor the AB concentration evolution at the midpoint (x=15 cm) along the tube. The results corresponding to the effect of these ARD parameters are shown in Figs. 6–8. Note that the results shown in Figs. 7 and 8 cover the range of Peclet number values from 0.056 to 1.78 (with  $L_{\rm Pe}=\Delta x=0.0625$  cm). With the fixed hybrid weight  $\omega=0.8$ , the PD solutions are smooth and stable (See Figs. 7 and 8).

From Fig. 6, we notice that the higher reaction rate  $R_{AB}$  leads to higher peaks on the product concentration curves at the mid-point, but this increase tends to saturate at the higher reaction rate values. Combined with Fig. 5, we know that the concentration peak cannot reach 0.01 mol/L (the maximum happens when  $R_{AB}$  tends to infinity). This is because the liquid is incompressible. Both A and B will be diluted when B flows into the tube, so that the maximum concentration of AB happens at the position where A and B are fully mixed and fully reacted. In other words, the concentrations of A and B cannot reach 0.01mol/L simultaneously, which means that the AB concentration cannot reach 0.01 mol/L. Fig. 6(a) also shows that the reaction rate has no effect on the time when the concentration reaches its peak value or when the product appears and vanishes at that location. A higher flow rate  $\nu$  makes the peak concentration happen earlier and earlier, as seen from Fig. 7, with the time ( $t_p$ ) for the concentration to reach its maximum at the tube's midpoint varies as x/V (x = 15 cm is the position of the midpoint), which is consistent with the analytical solution of the SPSM model shown in Eq. (37).

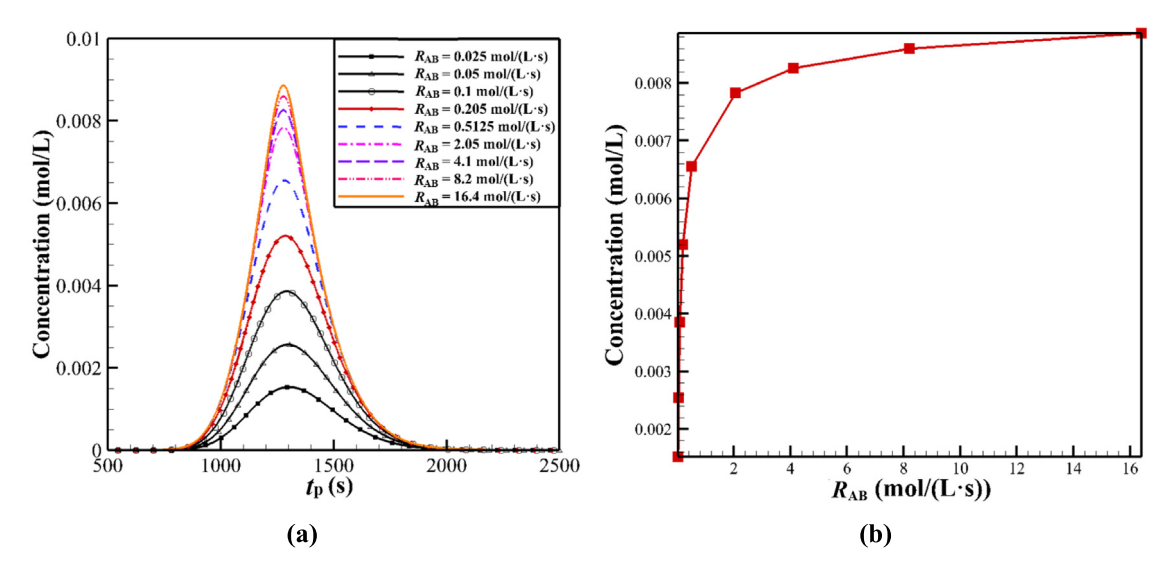


Fig. 6. (a) Time-evolution of the product AB's concentration at the midpoint (x = 15 cm) for different reaction rate  $R_{AB}$  values. D = 0.0017 cm<sup>2</sup>/s, and V = 0.0121 cm/s. (b) The AB concentration peak values at the midpoint versus the reaction rate.

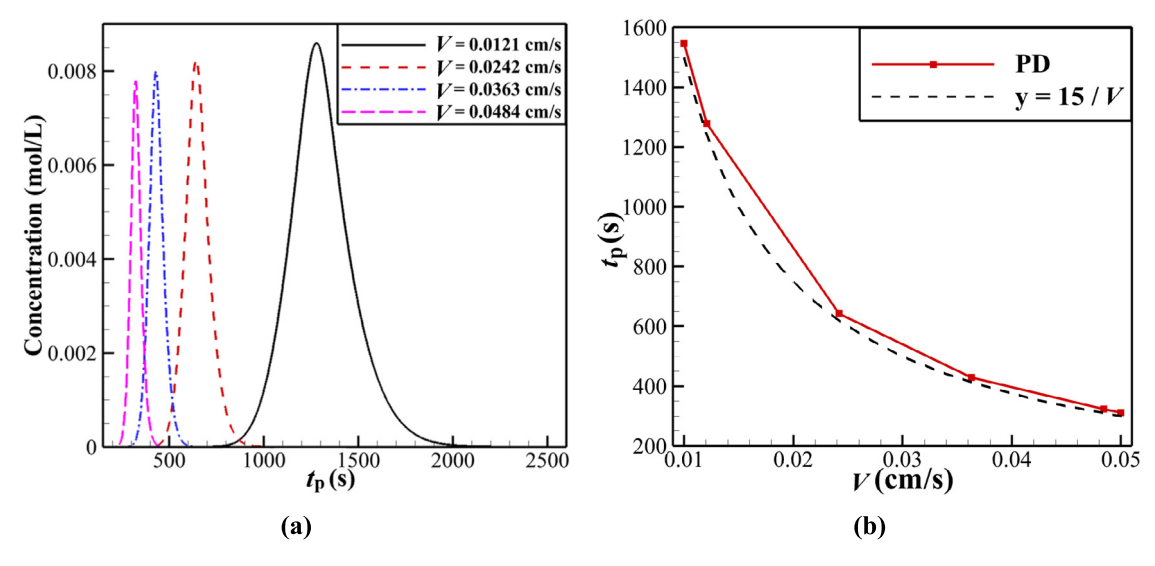


Fig. 7. (a) Time-evolution of the product AB's concentration at the midpoint (x = 15 cm) for different flow rates V. D = 0.0017 cm<sup>2</sup>/s, and  $R_{AB} = 16.4$  L/(mol s). (b) The variation of time for AB concentration at the midpoint to reach its maximum as a function of the flow rate.

Fig. 8 reveals that a higher diffusion coefficient D leads to a faster-moving rate of the highest AB concentration location, and  $t_p$  linearly depends on the diffusion coefficient. Figs. 15 and 16 in Appendix B imply that  $t_p$  is independent on  $\delta$ , but inversely proportional with m. The dotted line in Fig. 8(b) corresponds to the time x/V = 1239.7 s (x = 15 cm is the position of the midpoint). We expect that when D is much smaller than Vx and m goes to infinity,  $t_p$  will converge to x/V, which would be consistent with the SPSM method.

# 4.2. Examples of 2D bimolecular reactions

In Section 4.1, we have validated the PD reaction-diffusion model in 1D by comparing the simulated results against experimental measurements and the SPSM prediction. In this section, we use the model to solve bimolecular

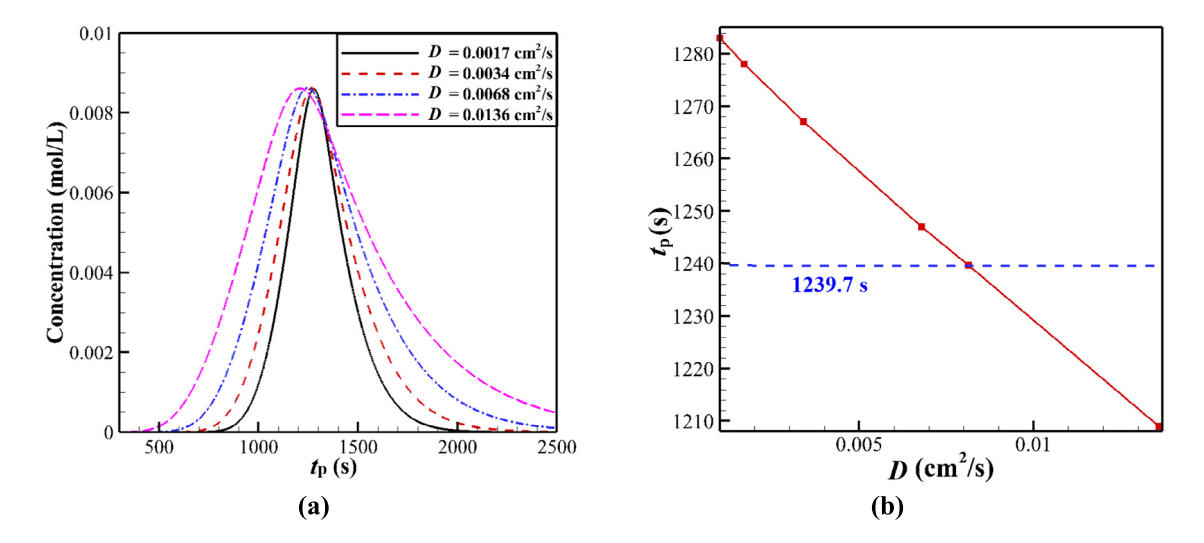


Fig. 8. (a) Evolution of the product AB's concentration at the midpoint (x = 15 cm) with different diffusion coefficient D. V = 0.0121 cm/s,  $R_{\rm AB} = 16.4 \text{ L/(mol s)}$ . (b) The time for AB concentration at the middle point to reach its maximum versus the diffusion coefficient.

ARD problems in 2D. The tests shown in this section are extensions of the advection-diffusion examples for a single solute shown in Ref. [55], to a bimolecular reaction with three solutes: two reactants and one product. The classical

partial differential equations for the ARD problem for bimolecular reaction in 2D are [55,56]: 
$$\begin{cases} \frac{\partial C_{A}}{\partial t} = D_{x} \frac{\partial^{2} C_{A}(x,y,t)}{\partial x^{2}} + D_{y} \frac{\partial^{2} C_{A}(x,y,t)}{\partial y^{2}} - V_{x} \frac{\partial C_{A}(x,y,t)}{\partial x} - R_{AB}C_{A}(x,y,t)C_{B}(x,y,t) \\ \frac{\partial C_{B}}{\partial t} = D_{x} \frac{\partial^{2} C_{B}(x,y,t)}{\partial x^{2}} + D_{y} \frac{\partial^{2} C_{B}(x,y,t)}{\partial y^{2}} - V_{x} \frac{\partial C_{B}(x,y,t)}{\partial x} - R_{AB}C_{A}(x,y,t)C_{B}(x,y,t) \\ \frac{\partial C_{AB}}{\partial t} = D_{x} \frac{\partial^{2} C_{AB}(x,y,t)}{\partial x^{2}} + D_{y} \frac{\partial^{2} C_{AB}(x,y,t)}{\partial y^{2}} - V_{x} \frac{\partial C_{AB}(x,y,t)}{\partial x} + R_{AB}C_{A}(x,y,t)C_{B}(x,y,t) \end{cases} , (38)$$

where  $D_x$  and  $D_y$  are the diffusion coefficients in the direction of x and y, respectively,  $V_x$  is the uniform flow rate in x-direction, and  $R_{AB}$  is the reaction rate. For all the examples (in square domains of side length L=30 cm) shown in this section, we set the diffusion coefficient in the x and y directions as  $D_x = D_y = 0.017 \text{ cm}^2/\text{s}$ ; the steady flow velocity in the x-direction as  $V = V_x = 0.0121$  cm/s; the reaction rate is  $R_{AB} = 8.2$  L/(mol s); based on the  $\delta$ -convergence and m-convergence studies shown in Appendix B, we use the horizon size  $\delta = L/60$  and horizon factor m = 4 and the grid spacing  $\Delta x = \delta/m = L/240$ .

### 4.2.1. ARD examples in 2D homogeneous media

First, we consider ARD processes in homogeneous media. Two cases are considered: in Case 1, from the left side, reactant B invades a square domain filled with reactant A and reacts with it to produce AB (see Fig. 9(a)), which is similar to the process of constantly pouring a purifying chemical into a polluted water flow; in Case 2, from the left side, reactants A and B simultaneously enter a square domain via different openings (see Fig. 9 (b)), which is similar to the reaction between a pollutant and a purifying chemical entering simultaneously into a water flow. In both cases, the top and bottom sides have zero-flux boundary conditions (the spatial derivatives of concentrations in the vertical direction are zero). In the PD nonlocal model, the zero-flux boundary conditions are automatically satisfied since there are no PD bonds across the zero-flux boundaries to exchange mass with. In both cases, the solvent, flowing in from the left side and flowing out on the right side, has a uniform flow rate imposed at all times in the x-direction. Under this directional flow setting, the chemicals on the right side keep flowing out from the square domain, and thus do not affect the concentration field inside the domain. Therefore, in the simulation, we set the right boundary to be free. The classical boundary conditions that the PD model will try to enforce on the

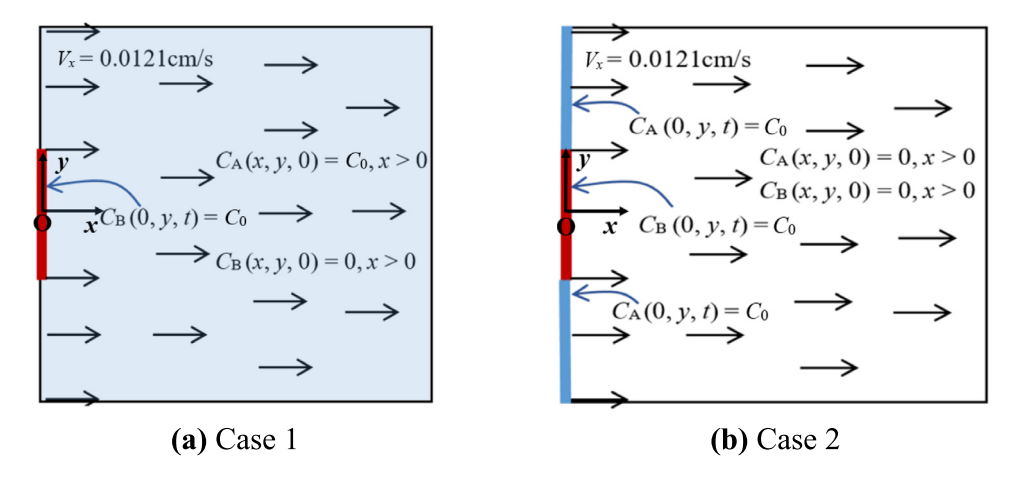


Fig. 9. Classical boundary and initial conditions for two bimolecular reaction cases of ARD: (a) reactant B flows into the square domain filled with A; (b) A and B flow into the square domain simultaneously with the same velocity. Top and bottom boundaries have zero flux, left and right boundaries have constant fluid velocity.

left side and the initial conditions for the case shown in Fig. 9(a) are:

$$\begin{cases} C_{A}(0, y, t) = 0, C_{B}(0, y, t) = 0, C_{AB}(0, y, t) = 0 & -\frac{L}{2} \le y \le -\frac{L}{6} \text{ or } \frac{L}{6} \le y \le \frac{L}{2}, t > 0 \\ C_{A}(0, y, t) = 0, C_{B}(0, y, t) = C_{0}, C_{AB}(0, y, t) = 0 & -\frac{L}{6} < y < \frac{L}{6}, t > 0 \\ C_{A}(x, y, t) = C_{0}, C_{B}(x, y, t) = C_{AB}(x, y, t) = 0 & t = 0 \end{cases}$$

$$(39)$$

The boundary conditions on the left side and the initial conditions for the case shown in Fig. 9(b) are:

$$\begin{cases} C_{A}(0, y, t) = C_{0}, C_{B}(0, y, t) = 0, C_{AB}(0, y, t) = 0 & -\frac{L}{2} \le y \le -\frac{L}{6} \text{ or } \frac{L}{6} \le y \le \frac{L}{2}, t > 0 \\ C_{A}(0, y, t) = 0, C_{B}(0, y, t) = C_{0}, C_{AB}(0, y, t) = 0 & -\frac{L}{6} < y < \frac{L}{6}, t > 0 \\ C_{A}(x, y, t) = C_{B}(x, y, t) = C_{AB}(x, y, t) = 0 & t = 0 \end{cases}$$

$$(40)$$

Fig. 10(a-c) show the results corresponding to Case 1, Fig. 9(a), and Fig. 10 (d-f) display the results corresponding to Case 2, Fig. 9(b).

Fig. 10(a) shows that reactant A (originally present in the domain) forms a concentration distribution with gradient due to flow, diffusion, and its consumption due to reaction in regions where it comes in contact with reactant B. Fig. 10(c) and Movie 1 shows that the product AB is generated where the two reactants meet, and the peak concentration of the product AB occurs near  $x = V_x t$ , y = 0, where the two reactants are consumed rapidly. This is consistent with our inference in Section 4.1 and the results for the 1D problems. But, in the 2D model, the species diffuse in two directions, leading to a much lower concentration peak value for the AB product. If reactant B (invading into the domain) were to enter the domain over the entire right side, the concentration peak of product AB would match the 1D results obtained in Section 4.1.

Fig. 10(d–f) shows the results from Case 2. Different from Case 1, Case 2 is similar to the process of purifying flowing polluted water, for which both reactant A and B flow into the region continuously from the left boundary, from different regions. Fig. 10(f) shows that the peak concentration of product AB occurs near the left boundary all the time. It should be noted that the peak concentration of product AB does not decrease with time. The results shown in Fig. 10(f) and Movie 2, indicate that the peak concentration range of product AB in the domain will continue to broaden, and the reactants A and B will be used up far from the left boundary.

These 2D tests of ARD show that the PD model can conveniently simulate bimolecular reaction processes in flowing media.

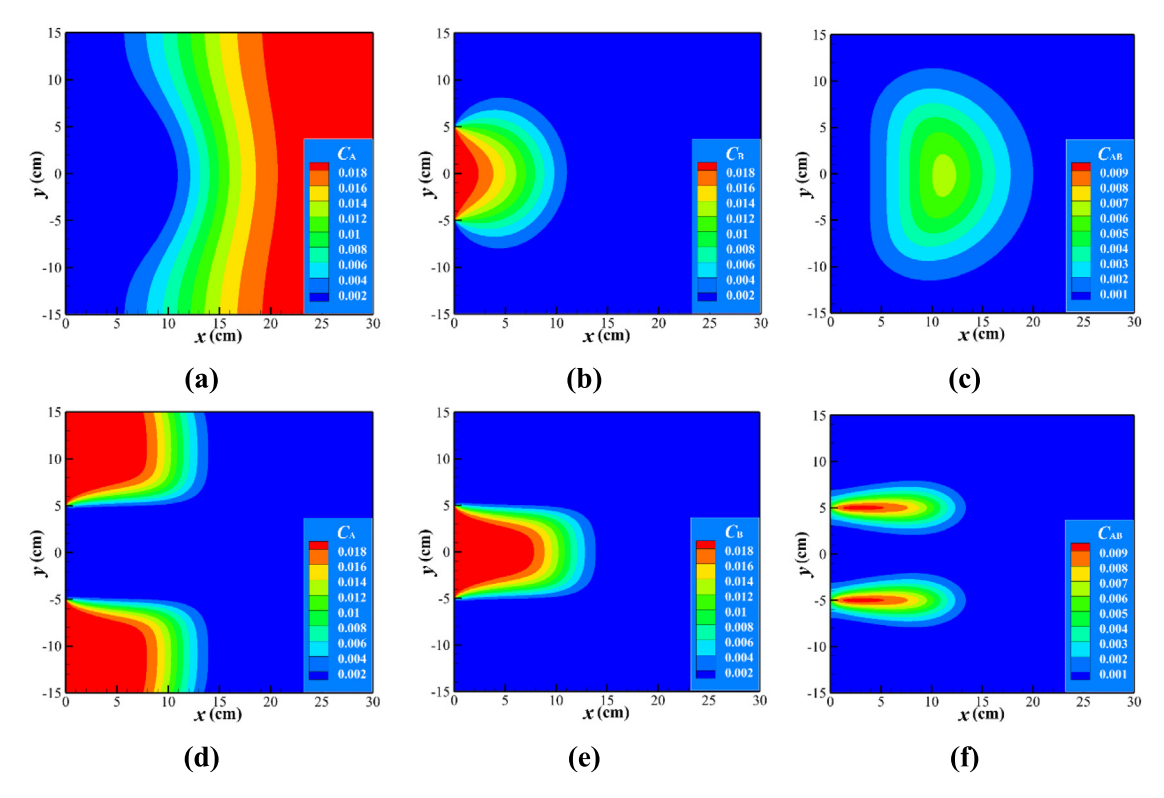


Fig. 10. Concentration distributions obtained by the new PD model at t = 916 s for Case 1 (top row) and Case 2 (bottom row): reactant A in (a) and (d), reactant B in (b) and (e), and reaction product AB in (c) and (f). Iteration time step  $\Delta t = 0.1$  s. See also Movies 1 and 2.

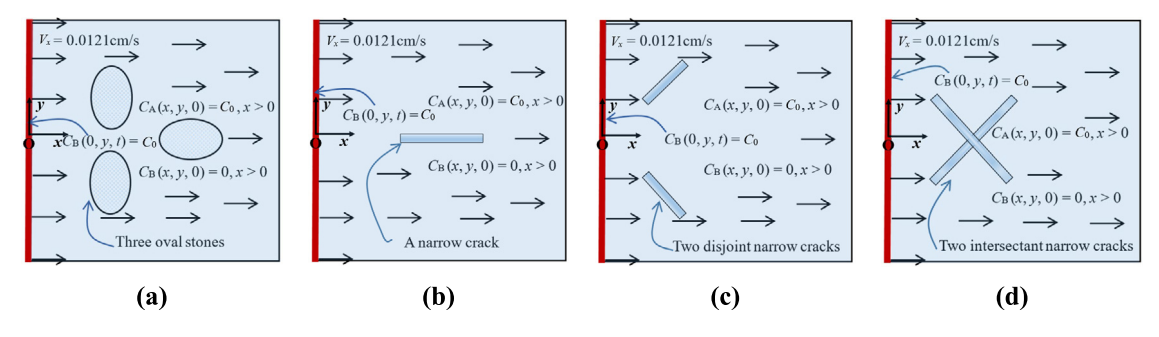


Fig. 11. Descriptions of 2D domains and initial and boundary conditions for ARD in heterogeneous media: (a) a domain with impermeable inclusions; (b-d) domains with different types of slit-like sinks (from which the solution can flow out).

### 4.2.2. Examples of ARD in 2D heterogeneous media

Most ARD processes in real life take place in complex, heterogeneous media. For instance, when polluted water flows underground, pollutants react or interact with chemicals in the ground with impermeable stones/rocks, which can significantly affect the advection-diffusion process of the polluted water and products. Another example is that of formaldehyde released from new furniture: as it diffuses into the indoor environment, reacts with oxygen, the furniture itself is a heterogeneous domain, while packages of activated carbon can be used to absorb the dangerous chemical, effectively acting as sinks for the hazardous specie. Metabolic processes in live organisms are further examples of ARD in heterogeneous media.

In this subsection, we show that the PD model can be applied to simulate ARD processes in heterogeneous media, including media with impermeable blocks and media with slit-like sinks. Four scenarios are considered, as shown in Fig. 11. All four cases share the same boundary and initial conditions: the top, bottom and right sides

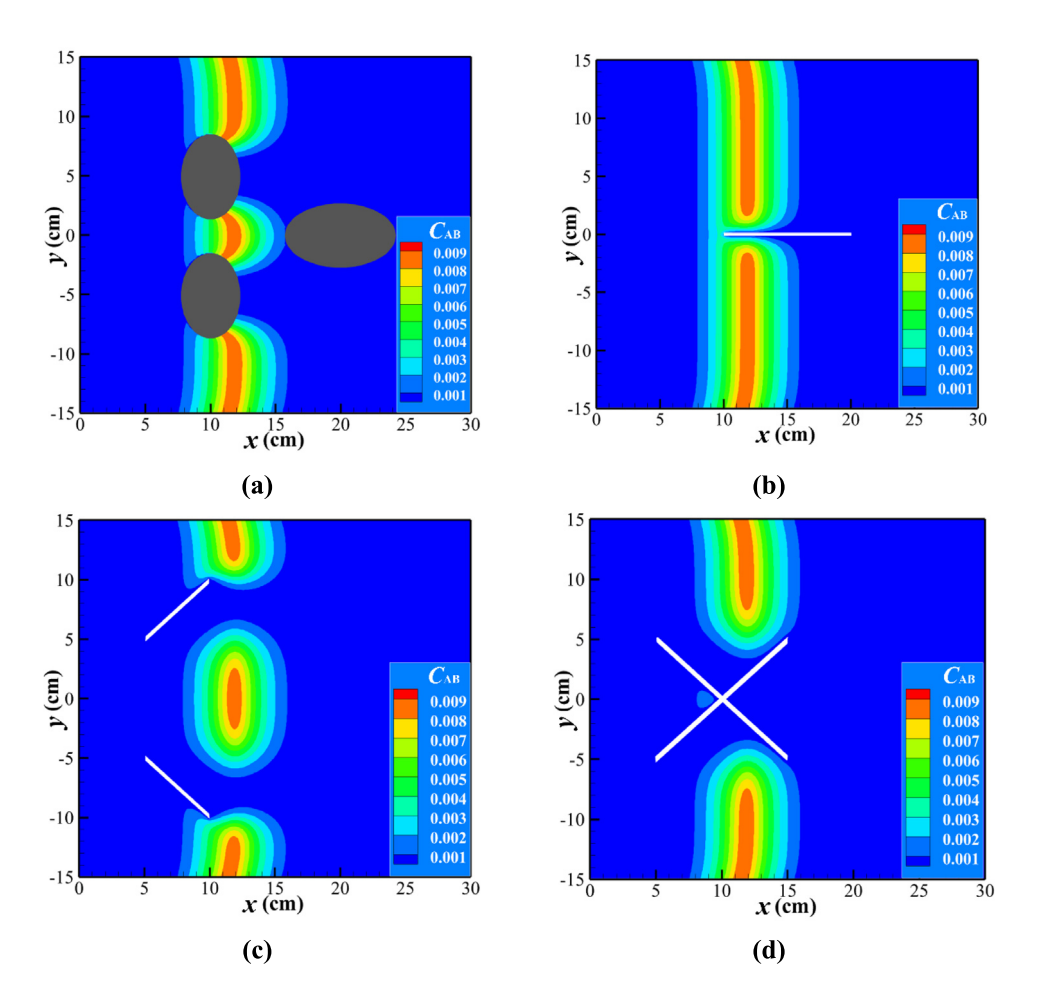


Fig. 12. Concentration distributions obtained by the PD model for the AB product at 1,000 s for the setups shown in Fig. 11: (a) ARD process in a domain with impermeable inclusions; (b-d) ARD process in domains with different types of crack-like sinks (from which the solution can flow out of the domain). Iteration time step  $\Delta t = 0.1$  s. See also Movies 3-6.

have the same boundary conditions as the ones applied in the cases shown in Section 4.2.1; the boundary conditions on the left side and the initial conditions are:

$$\begin{cases}
C_{A}(0, y, t) = 0, C_{B}(0, y, t) = C_{0}, C_{AB}(0, y, t) = 0 & t > 0 \\
C_{A}(x, y, t) = C_{0}, C_{B}(x, y, t) = C_{AB}(x, y, t) = 0 & t = 0
\end{cases}$$
(41)

In the simulations, with a uniform grid used over the entire domain, the impermeable blocks are implemented by breaking all PD diffusion bonds connected with the nodes of "stones"; the slit-like sinks are implemented by breaking all PD diffusion bonds across the sinks and setting all the concentrations of the nodes of sinks to be zero. In our examples, the width of the sinks is half of the horizon size.

Fig. 12 shows the snapshots of the product AB's concentration profile after 1,000 s, for all four cases shown in Fig. 11. The results (see also Movies 3–6) demonstrate that the PD model introduced here can easily address ARD processes in heterogeneous media, independent of the complexity of geometry and boundary conditions. The strong influence of impermeable blocks or crack-like sinks on the ARD process can help one design such features to eventually obtain desired reaction patterns.

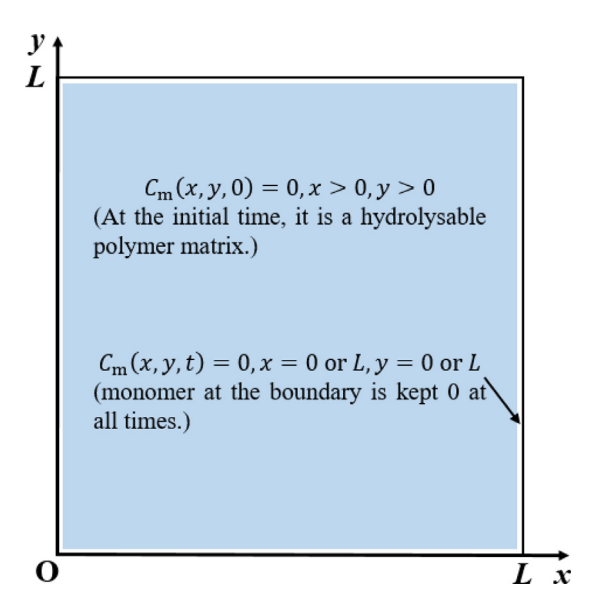


Fig. 13. Initial and boundary conditions for the hydrolysis reaction (following [64]).

### 4.3. Application to simulating the hydrolysis reaction

In Sections 4.1 and 4.2 we have seen how the PD model simulates ARD processes in which the reaction rate depends linearly on the local concentrations of the reactants. In this section, we investigate a hydrolysis reaction—diffusion example, in which a nonlinear dependence between the reaction rate and the local concentrations of the reactants (see Section 2.2) exists. Hydrolysis is the process of decomposition of macromolecular polymer into hydrolyzed monomers with smaller molecular weight under the action of water. Given the randomness of molecular weights of polymer chains, hydrolysis is a stochastic process in space.

Consider a square cross-section of a biodegradable implant, initially composed of some solid polymer (see Fig. 13, and [64]). The concentration of the reaction product (hydrolysis monomer) at the boundary of the domain is kept at zero at all times. The reaction happens at all points in the domain, but because of the stochastic process, some parts are fully reacted at different times compared with other locations. The concentration of hydrolysis monomer released by the node meeting the hydrolysis conditions is set to a dimensionless value of 1, namely the value of  $R_0$  in Eq. (11) is 1. The following input data is used in the simulations shown below (see [64]): degradation rate constant  $\lambda_0 = 8.41 \times 10^{-3} \text{day}^{-1}$ , diffusivity of hydrolyzate  $D_{\rm m}^0 = 0.87 \times 10^{-7} \text{ mm}^2 \text{s}^{-1}$ , constant  $S_{\rm m} = 8.52$ , and  $\beta = 3$ . Substituting these parameters into Eq. (11), the reaction term can be described as:

$$R(\mathbf{x},t) = \begin{cases} 0, & P_{R} \ge P_{H} \\ 1, & P_{R} < P_{H} \end{cases}, P_{H} = \frac{0.00841e^{-0.00841t} \left(1 + 3\left(e^{C_{m}-1}\right)\right)}{V_{0}V(t)}, 0 < P_{R} < 1, \tag{42}$$

Note that, as discussed in Section 2.2,  $P_R$  is a randomly generated number 0 and 1 (from a uniform probability distribution function), which mimics the randomness of molecular weight of polymer chains in a polymeric material. Different polymer systems may have specific probability distribution functions for their molecular structures of their chains, and in such cases, one simply uses those specific functions to generate the  $P_R$  values mentioned above to apply the model introduced here.

To study size effects, we consider two different matrix sizes for hydrolysis: Case 1: 3 mm  $\times$  3 mm and Case 2: 0.2 mm  $\times$  0.2 mm. For both cases,  $\Delta t = 86.4$  s. For Case 1,  $\delta = 0.05$  mm and m = 2; For Case 2,  $\delta = 0.01$  mm and m = 2. Fig. 14 shows the evolution of the degradation processes. The monomers are unevenly distributed across the domain at the early hydrolysis stage due to the stochastic reaction term, and later by the blocking from the remaining unhydrolyzed matrix. Along with the hydrolysis, the monomers have more pathways to diffuse out so that the concentration distribution of the monomers becomes smoother in time due to their faster out-diffusion.

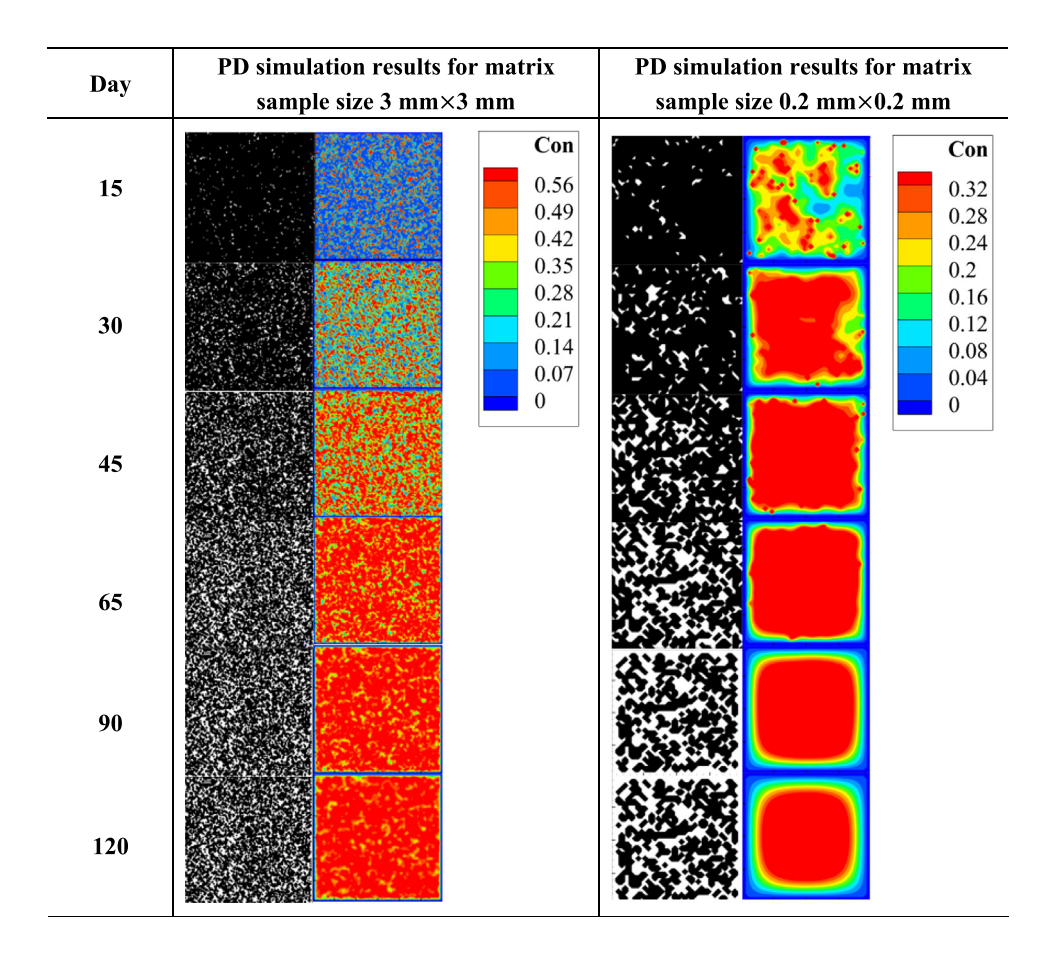


Fig. 14. PD simulation results of hydrolysis process of the hydrolyzable polymer matrix. In each set of PD results, the left column is the evolution of the remaining un-hydrolyzed matrix (solid polymer is black), and the right column is the evolution of the monomer concentration distribution. Iteration time step  $\Delta t = 86.4$  s. See also Movies 7 and 8.

As expected, by comparing hydrolysis with different cross-section sizes, we notice that the matrix with smaller cross-section hydrolyze faster. This is because the specific surface area decreases with increased cross-section. Note also that before hydrolysis, the polymer implant would undergo swelling, during which water diffuses into the polymer matrix. The current PD model does not, at this point, consider swelling of the implant, but this process can easily be incorporated.

The hydrolysis processes predicted by the PD model, as shown in Fig. 14, are in good agreement with the modeling results shown in Ref. [64], meaning that the PD model can also be applied to simulate the hydrolysis reaction. Comparing with the model shown in Ref. [64], the PD model can be used to treat the hydrolysis of polymer solids with damage and cracks.

While the flow simulations in the examples shown in this work used constant velocity flows, one could instead use the PD formulation of the Navier–Stokes equations from the recently published [72] and solve the fluid velocity as well. However, the focus of this work is on the reaction part of the general advection–reaction–diffusion problems, with specific applications to reactions between pollutants and cleaning agents in (underground) water flows and reactions related to polymer breakdown/degradation (hydrolysis). For many such problems, the assumption of constant fluid velocity seems a reasonable one. In the future, we are planning to use the formulations in [72] for the complete set of equations including the full Navier–Stokes equations solving for the fluid velocity field.

#### 5. Conclusions

In this paper, a peridynamic (PD) model was introduced for simulating advection-reaction-diffusion (ARD) processes. This expands an existing advection-diffusion model. The new model is very general, and depending on the type of chemical reactions, the reactions terms can be linear or nonlinear functions of the reactants' concentrations. The PD computational model can be applied to solve ARD problems in homogeneous and complex heterogeneous media, including cases with presence of obstacles, while using simple, uniform discretization grids.

We validated the model by comparing the PD results for an ARD example in 1D with a bimolecular reaction  $(A+B\to AB)$  with the corresponding experimental measurements and the approximate analytical solutions of the corresponding classical model. The model was then applied to simulate ARD processes in 2D domains (similar to purifying polluted flowing water via chemical reactions), including chemical reactions in heterogeneous media with impermeable inclusions.

The model can also be used to simulate and predict degradation of polymers (as in the case of dissolution of bio-degradable implants) induced by the hydrolysis reaction (M  $\rightarrow$   $\alpha$ m). The reaction involves a solid-to-liquid phase change, and the stochastic model was verified against published results on hydrolysis.

This paper aimed to provide a nonlocal platform for ARD simulations. Without presetting any functional variations across an interface, PD-based models can autonomously capture evolving interfaces with accuracy and ease. Besides the reactions presented in this paper, the PD platform can be applied for other physical-chemistry processes, such as corrosion of metal, solidification, charging and discharging in lithium batteries, etc.

# **Declaration of competing interest**

The authors declare that they have no known competing financial interests or personal relationships that could have appeared to influence the work reported in this paper.

# Data availability

No data was used for the research described in the article.

# Acknowledgments

This work was supported by the Natural Science Foundation of China (No. 11802098) and the Fundamental Research Funds for the Central Universities, China (HUST: YCJJ202203014, 2022JYCXJJ036 and No. 2021GCRC021). The work of F.B. was supported by the National Science Foundation (USA) award number 1953346.

## Appendix A. A dynamic solver for the peridynamic ARD equations

```
Dynamic solver for the peridynamic ARD equations
     (*Euler method, iterative loop, nt is the total number of iteration steps*)
2.
     for t = 1 to nt do
3.
       (*To solve the computing domain, n is the total number of nodes *)
4.
       for i = 1 to n do
5.
          for i = 1 to m do
6.
            (*Initialize \Delta C_i, m is the number of species of matter*)
7.
            \Delta C_i = 0
8.
            (*Determine the type of substance*)
9.
            \alpha = 1
10.
            if (resultant) then
11.
               \alpha = 0
12.
            end
13.
          End
```

```
14.
           (*obtaining the diffusion and advection term in the horizon*)
           (*fam is the number of nodes in the horizon*)
15.
16.
           for k = 1 to fam do
              for i = 1 to m do
17.
                 \Delta C_i = \Delta C_i + f_d \left( C_i^{t-1} \right) + f_v (C_i^{t-1})
18.
19.
20.
           End
21.
           (*Solve for the reaction terms*)
22.
           for i = 1 to m do
23.
              (* f_R is related to the actual reaction*)
              (*For example, for the bimolecular reaction, f_R = R_{AB}C_AC_B^*)
24.
              \Delta C_i = \Delta C_i + (-1)^{\alpha} f_R(C^{t-1})
25.
26.
           End
27.
        end
28.
        (*Update C_i, \Delta t is the time step size*)
29.
        for i = 1 to m do
           C_i^t = C_i^{t-1} + \Delta C_i \Delta t
30.
        End
31.
32.
     End
```

# Appendix B. Convergence analysis

m-convergence: With a fixed horizon size, L/60, we perform simulations with different m values. Fig. 15 shows the concentration distributions of product AB.

**δ-convergence:** For m = 4, we perform the δ-convergence tests. In Fig. 16, we plot the concentration distributions of product AB, for horizon sizes L/60, L/80, L/120, L/180, and L/240.

As shown in Figs. 15 and 16, the PD solutions fit well with the experimental measurements.

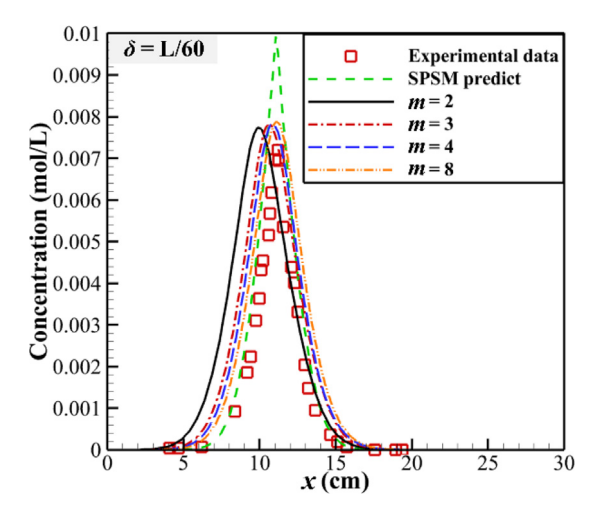


Fig. 15. The m-convergence study of 1D example.

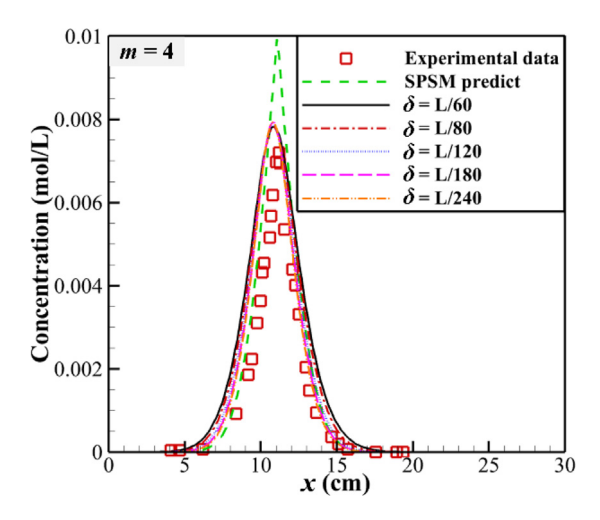


Fig. 16. The  $\delta$ -convergence study of 1D example (m = 4).

# Appendix C. Supplementary data

Supplementary material related to this article can be found online at https://doi.org/10.1016/j.cma.2023.116206.

#### References

- [1] Y. Wu, P. Wang, C. Hou, C. Liu, Z. Zhu, Turing patterns in a reaction-diffusion system, Commun. Theor. Phys. 45 (4) (2006) 761-764.
- [2] D.S. Raje, V. Kapoor, Experimental study of bimolecular reaction kinetics in porous media, Environ. Sci. Technol. 34 (7) (2000) 1234–1239.
- [3] Z. Chen, F. Bobaru, Selecting the kernel in a peridynamic formulation: A study for transient heat diffusion, Comput. Phys. Comm. 197 (2015) 51–60.
- [4] C. Cosner, Reaction-diffusion equations and ecological modeling, in: A. Friedman (Ed.), Tutorials in mathematical biosciences IV: evolution and ecology, Springer Berlin Heidelberg, Berlin, Heidelberg, 2008, pp. 77–115.
- [5] V. Guvanasen, R.E. Volker, Numerical solutions for solute transport in unconfined aquifers, Internat. J. Numer. Methods Fluids 3 (2) (1983) 103–123.
- [6] S. Kondo, T. Miura, Reaction-diffusion model as a framework for understanding biological pattern formation, Science 329 (5999) (2010) 1616–1620.
- [7] J. Naghipoor, N. Jafary, T. Rabczuk, Mathematical and computational modeling of drug release from an ocular iontophoretic drug delivery device, Int. J. Heat Mass Transfer 123 (2018) 1035–1049.
- [8] A.D. Rubio, A. Zalts, C.D. El Hasi, Numerical solution of the advection–reaction–diffusion equation at different scales, Environ. Model. Softw. 23 (1) (2008) 90–95.
- [9] F. Guillengonzalez, J.V. Gutierrezsantacreu, Error estimates of a linear decoupled Euler-FEM scheme for a mass diffusion model, Numer. Math. 117 (2) (2011) 333–371.
- [10] M. Dehghan, Weighted finite difference techniques for the one-dimensional advection-diffusion equation, Appl. Math. Comput. 147 (2) (2004) 307–319.
- [11] D.L. Young, Y.F. Wang, T.I. Eldho, Solution of the advection-diffusion equation using the Eulerian-Lagrangian boundary element method, Eng. Anal. Bound. Elem. 24 (6) (2000) 449–457.
- [12] C.L.N. Cunha, J.A.M. Carrer, M.F. Oliveira, V.L. Costa, A study concerning the solution of advection-diffusion problems by the boundary element method, Eng. Anal. Bound. Elem. 65 (2016) 79–94.
- [13] R. Metzler, J. Klafter, The random walk's guide to anomalous diffusion: A fractional dynamics approach, Phys. Rep. 339 (1) (2000) 1–77.
- [14] M. Yamaguchi, E. Yoshimoto, S. Kondo, Pattern regulation in the stripe of Zebrafish suggests an underlying dynamic and autonomous mechanism, Proc. Natl. Acad. Sci. USA 104 (12) (2007) 4790–4793.
- [15] G. Chen, Ballistic-diffusive equations for transient heat conduction from nano to macroscales, J. Heat Transfer-Trans. Asme 124 (2) (2002) 320–328.
- [16] F.X. Alvarez, D. Jou, Memory and nonlocal effects in heat transport: From diffusive to ballistic regimes, Appl. Phys. Lett. 90 (8) (2007) 083109.
- [17] D.Y. Tzou, Z.Y. Guo, Nonlocal behavior in thermal lagging, Int. J. Therm. Sci. 49 (7) (2010) 1133–1137.
- [18] S.A. Silling, Reformulation of elasticity theory for discontinuities and long-range forces, J. Mech. Phys. Solids 48 (1) (2000) 175–209.
- [19] A. Eringen, J. Wegner, Nonlocal continuum field theories, Appl. Mech. Rev. 56 (2) (2003) B20-B21.

- [20] F. Bobaru, J.T. Foster, P.H. Geubelle, S.A. Silling, Handbook of Peridynamic Modeling, Chapman and Hall/CRC, New York, 2016.
- [21] T. Mei, J. Zhao, Z. Liu, X. Peng, F. Bobaru, The role of boundary conditions on convergence properties of peridynamic model for transient heat transfer, J. Sci. Comput. 87 (2) (2021) 50–72.
- [22] F. Bobaru, M. Duangpanya, A peridynamic formulation for transient heat conduction in bodies with evolving discontinuities, J. Comput. Phys. 231 (7) (2012) 2764–2785.
- [23] W. Hu, Y.D. Ha, F. Bobaru, Peridynamic model for dynamic fracture in unidirectional fiber-reinforced composites, Comput. Methods Appl. Mech. Eng. 217-220 (2012) 247–261.
- [24] W. Hu, Y. Wang, J. Yu, C.-F. Yen, F. Bobaru, Impact damage on a thin glass plate with a thin polycarbonate backing, Int. J. Impact Eng. 62 (2013) 152–165.
- [25] S. Jafarzadeh, L. Wang, A. Larios, F. Bobaru, A fast convolution-based method for peridynamic transient diffusion in arbitrary domains, Comput. Methods Appl. Mech. Engrg. 375 (2021) 113633.
- [26] S. Jafarzadeh, F. Mousavi, A. Larios, F. Bobaru, A general and fast convolution-based method for peridynamics: Applications to elasticity and brittle fracture, Comput. Methods Appl. Mech. Engrg. 392 (2022) 114666.
- [27] S.A. Silling, E. Askari, A meshfree method based on the peridynamic model of solid mechanics, Comput. Struct. 83 (17–18) (2005) 1526–1535.
- [28] R.W. Macek, S.A. Silling, Peridynamics via finite element analysis, Finite Elem. Anal. Des. 43 (15) (2007) 1169–1178.
- [29] M.S. Breitenfeld, P.H. Geubelle, O. Weckner, S.A. Silling, Non-ordinary state-based peridynamic analysis of stationary crack problems, Comput. Methods Appl. Mech. Engrg. 272 (2014) 233–250.
- [30] P. Wu, F. Yang, Z. Chen, F. Bobaru, Stochastically homogenized peridynamic model for dynamic fracture analysis of concrete, Eng. Fract. Mech. 253 (2021) 107863.
- [31] J. Xu, A. Askari, O. Weckner, S.A. Silling, Peridynamic analysis of impact damage in composite laminates, J. Aerosp. Eng. 21 (3) (2008) 187–194.
- [32] B. Kilic, A. Agwai, E. Madenci, Peridynamic theory for progressive damage prediction in center-cracked composite laminates, Compos. Struct. 90 (2) (2009) 141–151.
- [33] W. Hu, Y.D. Ha, F. Bobaru, Modeling dynamic fracture and damage in a fiber-reinforced composite lamina with peridynamics, Int. J. Multiscale Comput. Eng. 9 (6) (2011) 707–726.
- [34] J. Mehrmashhadi, Z. Chen, J. Zhao, F. Bobaru, A stochastically homogenized peridynamic model for intraply fracture in fiber-reinforced composites, Compos. Sci. Technol. 182 (0266–3538) (2019) 107770.
- [35] Z. Cheng, Z. Fu, Y. Zhang, H. Wu, A peridynamic model for analyzing fracture behavior of functionally graded materials used as an interlayer, Acta Mech. Solida Sin. 33 (6) (2020) 781–792.
- [36] T.L. Warren, S.A. Silling, A. Askari, O. Weckner, M.A. Epton, J. Xu, A non-ordinary state-based peridynamic method to model solid material deformation and fracture, Int. J. Solids Struct. 46 (5) (2009) 1186–1195.
- [37] J.T. Foster, S.A. Silling, W.W. Chen, Viscoplasticity using peridynamics, Internat. J. Numer. Methods Engrg. 81 (10) (2010) 1242–1258.
- [38] E. Madenci, S. Oterkus, Ordinary state-based peridynamics for plastic deformation according to von Mises yield criteria with isotropic hardening, J. Mech. Phys. Solids 86 (2016) 192–219.
- [39] H. Ouchi, A. Katiyar, J. York, J.T. Foster, M.M. Sharma, A fully coupled porous flow and geomechanics model for fluid driven cracks: A peridynamics approach, Comput. Mech. 55 (3) (2015) 561–576.
- [40] S.A. Silling, F. Bobaru, Peridynamic modeling of membranes and fibers, Int. J. Non-Linear Mech. 40 (2-3) (2005) 395-409.
- [41] F. Bobaru, Influence of van der Waals forces on increasing the strength and toughness in dynamic fracture of nanofibre networks: A peridynamic approach, Modelling Simul. Mater. Sci. Eng. 15 (5) (2007) 397–417.
- [42] W. Dong, H. Liu, J. Du, X. Zhang, M. Huang, Z. Li, Z. Chen, F. Bobaru, A peridynamic approach to solving general discrete dislocation dynamics problems in plasticity and fracture: Part I, model description and verification, Int. J. Plast. 157 (2022) 103401.
- [43] W. Gerstle, S. Silling, D. Read, V. Tewary, R. Lehoucq, Peridynamic simulation of electromigration, Comput. Mater. Continua 8 (2) (2008) 75–92.
- [44] F. Bobaru, M. Duangpanya, The peridynamic formulation for transient heat conduction, Int. J. Heat Mass Transfer 53 (19–20) (2010) 4047–4059.
- [45] Z. Chen, F. Bobaru, Peridynamic modeling of pitting corrosion damage, J. Mech. Phys. Solids 78 (2015) 352-381.
- [46] S. Jafarzadeh, Z. Chen, F. Bobaru, Peridynamic modeling of repassivation in pitting corrosion of stainless steel, Corrosion 74 (4) (2017) 393–414.
- [47] Z. Chen, S. Jafarzadeh, J. Zhao, F. Bobaru, A coupled mechano-chemical peridynamic model for pit-to-crack transition in stress-corrosion cracking, J. Mech. Phys. Solids 146 (2021) 104203.
- [48] J.M. Zhao, S. Jafarzadeh, M. Rahmani, Z.G. Chen, Y.R. Kim, F. Bobaru, A peridynamic model for galvanic corrosion and fracture, Electrochim. Acta 391 (2021) 138968.
- [49] S. Fan, C. Tian, Y. Liu, Z. Chen, Surface stability in stress-assisted corrosion: A peridynamic investigation, Electrochim. Acta 423 (2022) 140570.
- [50] K. Dayal, K. Bhattacharya, Kinetics of phase transformations in the peridynamic formulation of continuum mechanics, J. Mech. Phys. Solids 54 (9) (2006) 1811–1842.
- [51] Q. Du, M. Gunzburger, R.B. Lehoucq, K. Zhou, Analysis and approximation of nonlocal diffusion problems with volume constraints, Soc. Ind. Appl. Math. 54 (4) (2012) 667–696.
- [52] S. Oterkus, E. Madenci, A. Agwai, Peridynamic thermal diffusion, J. Comput. Phys. 265 (2014) 71-96.
- [53] S.A. Silling, M. Epton, O. Weckner, J. Xu, E. Askari, Peridynamic states and constitutive modeling, J. Elasticity 88 (2) (2007) 151–184.
- [54] A. Katiyar, S. Agrawal, H. Ouchi, P. Seleson, J.T. Foster, M.M. Sharma, A general peridynamics model for multiphase transport of non-Newtonian compressible fluids in porous media, J. Comput. Phys. (2020) 402.

- [55] J. Zhao, Z. Chen, J. Mehrmashhadi, F. Bobaru, Construction of a peridynamic model for transient advection-diffusion problems, Int. J. Heat Mass Transfer 126 (2018) 1253–1266.
- [56] C.M. Gramling, C.F. Harvey, L.C. Meigs, Reactive transport in porous media: A comparison of model prediction with laboratory visualization, Environ. Sci. Technol. 36 (11) (2002) 2508–2514.
- [57] X. Wang, B. Wang, M. Meyerson, C.B. Mullins, Y. Fu, L. Zhu, L. Chen, A phase-field model integrating reaction-diffusion kinetics and elasto-plastic deformation with application to lithiated selenium-doped germanium electrodes, Int. J. Mech. Sci. (2018) 158–171.
- [58] M. Ohno, K. Matsuura, Diffusion-controlled peritectic reaction process in carbon steel analyzed by quantitative phase-field simulation, Acta Mater. 58 (18) (2010) 6134–6141.
- [59] S. Jafarzadeh, Z. Chen, J. Zhao, F. Bobaru, Pitting, lacy covers, and pit merger in stainless steel: 3D peridynamic models, Corros. Sci. 150 (2019) 17–31.
- [60] Y. Liu, F. Yang, W. Zhou, Z. Chen, F. Bobaru, Peridynamic modeling of early-age cracking behaviour in continuously reinforced concrete pavement, Int. J. Pavement Eng. (2022) 1–19.
- [61] S. Patankar, Numerical Heat Transfer and Fluid Flow, CRC Press, 1980, Chapter 5.
- [62] P. Wu, J. Zhao, Z. Chen, F. Bobaru, Validation of a stochastically homogenized peridynamic model for quasi-static fracture in concrete, Eng. Fract. Mech. 237 (2020) 107293.
- [63] A. Göpferich, Polymer bulk erosion, Macromolecules 30 (9) (1997) 2598-2604.
- [64] Y. Chen, S. Zhou, Q. Li, Mathematical modeling of degradation for bulk-erosive polymers: Applications in tissue engineering scaffolds and drug delivery systems, Acta Biomater 7 (3) (2011) 1140–1149.
- [65] Z. Zhou, X. Peng, P. Wu, Z. Chen, F. Bobaru, New insights on convergence properties of peridynamic models for transient diffusion and elastodynamics, Commun. Comput. Phys. 32 (2022) 1257–1286.
- [66] Z. Chen, X. Peng, S. Jafarzadeh, F. Bobaru, Analytical solutions of peridynamic equations. Part I: Transient heat diffusion, J. Peridyn. Nonlocal Model. 4 (3) (2022) 303–335.
- [67] F. Bobaru, G. Zhang, Why do cracks branch? A peridynamic investigation of dynamic brittle fracture, Int. J. Fract. 196 (1–2) (2015) 59–98.
- [68] F. Scabbia, C. Gasparrini, M. Zaccariotto, U. Galvanetto, A. Larios, F. Bobaru, Moving interfaces in peridynamic diffusion models and the influence of discontinuous initial conditions: Numerical stability and convergence, Comput. Math. Appl. (2023) forthcoming, Available at http://dx.doi.org/10.2139/ssrn.4458848.
- [69] J. Zhao, S. Jafarzadeh, Z. Chen, F. Bobaru, An algorithm for imposing local boundary conditions in peridynamic models on arbitrary domains, 2020, engrXiv Preprint http://dx.doi.org/10.31224/osf.io/7z8qr.
- [70] H. Yan, M. Sedighi, A.P. Jivkov, Peridynamics modelling of coupled water flow and chemical transport in unsaturated porous media, J. Hydrol. 591 (2020) 125648.
- [71] O.V. Le, F. Bobaru, Surface corrections for peridynamic models in elasticity and fracture, Comput. Mech. 61 (2018) 499-518.
- [72] J. Zhao, A. Larios, F. Bobaru, Construction of a peridynamic model for viscous flow, J. Comput. Phys. 468 (2022) 111509.